

# **A Tsunami Forecast Model For Bar Harbor, Maine**

**Stewart Allen**

## **Table of Contents**

<b>Abstract</b>	<b>3</b>
<b>1.0 Background and Objectives</b>	<b>3</b>
<b>2.0 Forecast Methodology</b>	<b>4</b>
<b>3.0 Model Development</b>	<b>5</b>
<b>3.1. Forecast Area</b>	<b>5</b>
<b>3.2. Historical Events and Tide Gauge Records</b>	<b>6</b>
<b>3.3. Model Setup</b>	<b>7</b>
<b>3.4. Synthetic Scenarios</b>	<b>9</b>
<b>3.5. Historical Event Scenarios</b>	<b>9</b>
<b>4.0 Results and Discussion</b>	<b>9</b>
<b>4.1. Results from the Synthetic Micro Scenario</b>	<b>9</b>
<b>4.2. Results from Other Synthetic Scenarios</b>	<b>10</b>
<b>4.3. Results from the Historical Event Scenario</b>	<b>11</b>
<b>4.4. Discussion</b>	<b>12</b>
<b>5.0 Summary and Conclusions</b>	<b>13</b>
<b>6.0 Acknowledgments</b>	<b>13</b>
<b>7.0 References</b>	<b>13</b>
<b>Tables</b>	<b>16</b>
<b>Figures</b>	<b>16</b>
<b>Appendix A</b>	<b>18</b>
<b>A.1 Reference model *.in file</b>	<b>18</b>
<b>A.2 Forecast Model *.in file</b>	<b>18</b>
<b>Appendix B</b>	<b>19</b>
<b>Appendix C Description of Indices</b>	<b>20</b>
<b>C.1 Normalised error in the maximum amplitude</b>	<b>20</b>
<b>C.2 Pearson correlation coefficient</b>	<b>20</b>
<b>C.3 Normalised Root-mean-square error</b>	<b>21</b>
<b>C.4 Index of Agreement</b>	<b>21</b>
<b>C.5 Watterson's transformed Mielke index</b>	<b>21</b>
<b>C.6 Mielke and Berry index</b>	<b>22</b>



# Abstract

This report outlines the steps taken to generate a tsunami forecast model for Bar Harbor, Maine. An outline of the steps taken to produce the bathymetric grids is provided. Following that, the model is tested using a number of synthetic scenarios and one historical scenario.

The scenarios revealed that the low-resolution forecast model performs well at reproducing the arrival of tsunamis, the first few waves and the ongoing low-frequency characteristics simulated in the high-resolution reference models. However it is unable to accurately maintain the high-frequency variations that are evident in the reference model. Given that this variability predominantly occurs in very shallow and coastal areas (i.e. the regions of greatest interest from a forecast perspective), it suggests that the forecast model is predisposed to underestimating the potential impacts in these areas.

## 1.0 Background and Objectives

The Pacific Marine Environmental Laboratory (PMEL) of the National Oceanic and Atmospheric Administration (NOAA) Center for Tsunami Research (NCTR) has developed tsunami forecasting capability for operational use by NOAA's Tsunami Warning Centers located in Hawaii and Alaska (Titov et al. 2005). The system is designed to efficiently provide basin-wide warning of approaching tsunami waves. The system, termed Short-term Inundation Forecast of Tsunamis (SIFT), combines real-time tsunami event data with numerical models to produce estimates of tsunami arrival times, amplitudes and inundations at coastal communities of interest. The SIFT system integrates several key components: deep-ocean, real-time observations of tsunamis, a basin-wide pre-computed propagation database (Gica, et al., 2009) of water level and flow velocities based on potential seismic unit sources, an inversion algorithm to refine the tsunami source based on deep-ocean observations during an event, and optimized tsunami forecast models.

Bar Harbor is a coastal town of the state of Maine and is situated on the North Eastern shore of Mount Desert Island. As of the 2009 US census<sup>1</sup>, it had approximately 5200 inhabitants. It is a popular summer holiday destination and during that period, its population swells to tens-of-thousands of inhabitants<sup>2</sup>. The nearby Acadia National Park, which surrounds Bar Harbor and incorporates several nearby islands, receives an estimated 2 million visitors annually<sup>3</sup>. The relatively sheltered, natural waters of Frenchman Bay mean that recreational maritime activities are also prevalent in Bar Harbor with many cruise ships visiting each year. Therefore, Bar Harbor was selected for the construction of a tsunami forecast model due to this popularity as a tourist destination.

This report details the development of a high-resolution tsunami forecast model for Bar Harbor. It includes a description of the development of the bathymetric grids, followed by stability testing and model validation with a set of synthetic events (given the absence of historical data).

---

<sup>1</sup> <http://www.census.gov/popest/data/index.html>

<sup>2</sup> <http://www.barharbormaine.gov/xhtml/121/ViewDefault/>

<sup>3</sup> <http://www.nps.gov/acad/parkmgmt/statistics.htm>

## 2.0 Forecast Methodology

A high-resolution inundation model is used as the basis for the development of a tsunami forecast model to operationally provide estimates of wave arrival time, wave height, and inundation at Bar Harbor, Maine following tsunami generation. All tsunami forecast models are run in real time while a tsunami is propagating across the open ocean. The Bar Harbor model was designed and tested to perform under stringent time constraints given that time is generally the single limiting factor in saving lives and property. The goal of this work is to maximize the length of time that the community of Bar Harbor has to react to a tsunami threat by providing accurate information quickly to emergency managers and other officials responsible for warning the community and protecting infrastructure.

The general tsunami forecast model, based on the Method of Splitting Tsunami (MOST), is used in the tsunami inundation and forecasting system to provide real-time tsunami forecasts at selected coastal communities. The model runs in minutes while employing high-resolution grids constructed by the National Geophysical Data Center (NGDC). The Method of Splitting Tsunami (MOST) is a suite of numerical simulation codes capable of simulating three processes of tsunami evolution: generation by earthquake, transoceanic propagation, and inundation of dry land. The MOST model has been extensively tested against a number of laboratory experiments and benchmarks (Synolakis et al., 2008) and was successfully used for simulations of many historical tsunami events. The main objective of a forecast model is to provide an accurate, yet rapid, estimate of wave arrival time, wave height, and inundation in the minutes following a tsunami event. Titov and González (1997) describe the technical aspects of forecast model development, stability, testing, and robustness, and Tang et al. (2009) provide detailed forecast methodology.

A basin-wide database of pre-computed water elevations and flow velocities for unit sources covering worldwide subduction zones has been generated to expedite forecasts (Gica et al., 2008). As the tsunami wave propagates across the ocean and successively reaches tsunameter observation sites, recorded sea level is ingested into the tsunami forecast application in near real-time and incorporated into an inversion algorithm to produce an improved estimate of the tsunami source. A linear combination of the pre-computed database is then performed based on this tsunami source, now reflecting the transfer of energy to the fluid body, to produce synthetic boundary conditions of water elevation and flow velocities to initiate the forecast model computation.

Accurate forecasting of the tsunami impact on a coastal community largely relies on the accuracies of bathymetry and topography and the numerical computation. The high spatial and temporal grid resolution necessary for accurate modeling poses a challenge to the run-time requirement for real-time forecasts. Each forecast model consists of three telescoped grids with increasing spatial resolution to the finest grid, and temporal resolution for simulation of wave inundation onto dry land. The forecast model utilizes the most recent bathymetry and topography available to reproduce the correct wave dynamics during the inundation computation. Forecast models, including the Bar Harbor model, are constructed for at-risk populous coastal communities in the Pacific and Atlantic Oceans. Previous and present development of forecast models in the Pacific (Titov et al., 2005; Titov, 2009; Tang et al., 2008; Wei et al., 2008) have validated the accuracy and efficiency of each forecast model currently implemented in the real-time tsunami forecast system. Models are tested when the opportunity arises and are used for scientific research. Tang et al. (2009) provide forecast methodology details.

## 3.0 Model Development

Modeling of coastal communities is accomplished by development of a set of three nested grids that telescope down from a large spatial extent to a grid that finely defines the localized community. The basis for these grids is a high-resolution digital elevation model constructed by either NCTR or, more commonly, by NGDC using best available bathymetric, topographic, and coastal shoreline data for an at-risk community. For each community, data are compiled from a variety of sources to produce a digital elevation model referenced to Mean High Water in the vertical and to the World Geodetic System 1984 in the horizontal<sup>4</sup>. From these digital elevation models, a set of three high-resolution reference models are constructed and then “optimized” to run within an operationally specified period of time (specifically 4 hours of simulation should be completed within 10 minutes of wall-clock time).

### 3.1. Forecast Area

The local bathymetry of the region surrounding Bar Harbor is relatively complex. The region is situated within the Gulf of Maine, which is approximately 420 km (260 miles) wide at its ‘mouth’ (i.e. the eastern extremity of Cape Cod to the southern point on Cape Sable Island, Nova Scotia; see Figure 1). From the line that transects this mouth, it is approximately 200 km (125 miles) to the inner coastline of the gulf. The gulf is entirely on the North American eastern continental shelf, which is relatively wide, extending on the order of 320 to 440 km (200 to 275 miles) from the coastline in this region. Water depths beyond the continental shelf rise from approximately 5000 m to 2000 m near the continental margin. On the shelf, water depths are approximately 100 to 200 m in the Gulf of Maine. However, there is an elevated region, the Georges Bank, situated near the shelf edge. It is 240 km (50 miles) in length and 120 km (75 miles) in width and is submerged to depths ranging from several meters to several dozen meters. This feature affords a degree of protection to the Gulf of Maine from incoming tsunamis. There are two deeper channels at either end of the Georges Bank, the Northeast Channel (200 to 250 m or 650 to 820 ft deep) and the Great South Channel (50 to 100 m or 160 to 320 ft deep). A map of the Gulf of Maine, with key features indicated is shown in Figure 1.

Bar Harbor is located on the western shores of Frenchman Bay, which, in turn, is located on the northern shores of the Gulf of Maine. The mouth of Frenchman Bay is approximately 8 km (5 miles) wide and it roughly maintains this width over its 15 km (9 miles) length. Bar Harbor is located approximately 8 km (5 miles) from the bay mouth. A map of Frenchman Bay, with key features and locations indicated, is shown in Figure 2. The features and locations indicated in this figure will be referred to regularly throughout this study. Composited aerial photography of the region is shown in Figure 3 and an oblique view of Bar Harbor and surrounds is shown in Figure 4.

There are many islands of varying size within Frenchman Bay. Those of most significance to Bar Harbor are known as the Porcupine Group and consists of 5 main islands and several smaller outcrops. In particular, the southern most island of the group, known as Bald Porcupine Island, features an artificial breakwater. Constructed in 1917, it extends southwest from the island some 800 meters (2600 feet) towards the coast, leaving a narrow, shallow

---

<sup>4</sup> <http://ngdc.noaa.gov/mgg/inundation/tsunami/inundation.html>

channel 200m (700 feet) wide. On the eastern side of Bald Porcupine island, there is a deeper, wider channel that is around 1600 m (1 mile) wide and as deep as 70m (230 ft).

Bar Harbor itself is tucked away in a narrow channel 500m (188ft) wide to the south of Bar Island. The waters of this channel are very shallow, being mostly less than 5m (16ft) in depth. At the western end of this channel, there is a natural, intertidal sand bar connecting Bar Harbor and Bar Island. At low tide, this sand bar is exposed, allowing pedestrian and limited vehicular access to Bar Island (However, recall that this study is conducted using a digital elevation model referenced to Mean High Water, meaning this sand bar remains entirely submerged in the model). Human activity on this sand bar and in other inter-tidal zones in the area means that should a tsunami arrive at Bar Harbor during low tide, it may be particularly hazardous.

There are a number of artificial structures within Bar Harbor that have been constructed to support recreational maritime activities. Some of these are solid (i.e. neither on footings nor are floating) and are large enough to be resolved by the tsunami model. Others are open and on pylons. These are not included in the model.

## **3.2. Historical Events and Tide Gauge Records**

There is a tide gauge located on a pier in Bar Harbor. The gauge is owned and operated by the National Ocean Service, which has assigned the gauge assigned reference identifiers of ATGM1/8413320. It was established in August 1947 with its present instrumentation installed in June 1999. It has verified hourly records going back to March 1950. Characteristics of the tide gauge are given in Table 1 and a photo of the instrumentation housing is shown in Figure 5. The location of the gauge is indicated on Figure 2 and this point will serve as the ‘warning point’ for the models – that is, time series at the model grid point nearest the tide gauge will be evaluated. The coordinates of the grid node in each model that is nearest to the tide gauge’s location is also given in Table 1.

Although tsunamis have occurred in the Atlantic basin in the past, generated both seismically and by other mechanisms, there have been no historical observations of tsunamis by the Bar Harbor tide gauge.

The most significant recorded earthquake and tsunami to have occurred in the Atlantic Ocean was the Great Lisbon Earthquake of 1 November 1755, a large earthquake that occurred approximately 200km from the Atlantic coastline of Portugal. Not only did the earthquake cause significant damage close to the epicenter, it generated a tsunami that was locally destructive on the Portuguese coast over a considerable area. The death toll in Portugal, Spain and Morocco was estimated to be well in excess of 100,000 people (Chester, 2001).

There were some observations of this tsunami on the east coast of the United States, as far north as Boston, Massachusetts (Barkan et al., 2009). However, no known direct observations exist for the Bar Harbor region. Although European settlement of Bar Harbor didn’t occur until 1763, there are also no known accounts from members of the Wabanaki Nation, the indigenous peoples of the region. It is thought that some paleo-records of tsunami deposits may exist, from which any tsunami-related inundation might be deduced. However if these proxy records exist, they were not available for this study.

The moment magnitude of the Great Lisbon Earthquake estimated by modern seismology to be on the order of  $M_w$  8.5 to 9.0. This was determined using known seismology of the

suspected source region, geophysical surveys and tsunami simulations (e.g. Gutscher et al., 2006; Barkan et al., 2009).

### 3.3. Model Setup

The general methodology for modeling at-risk coastal communities is to develop a set of three nested grids, referred to as the A-, B-, and C-grids, each of which becomes successively finer in resolution as they telescope into the primary region of interest, where the major population, economic and infrastructural centers of the community are located. The offshore area is covered by the largest and lowest resolution A-grid while the near-shore details are resolved within the finest scale C-grid to the point that tide gauge observations recorded during historical tsunamis (where available) are resolved within acceptable accuracy limits.

The procedure is to begin development with large spatial extent merged bathymetric and topographic grids at high resolution. The basis for these grids is a high-resolution digital elevation model constructed by NGDC and NCTR using all available bathymetric, topographic, and shoreline data. For each community, data are compiled from a variety of sources to produce a digital elevation model referenced to Mean High Water in the vertical and to the World Geodetic System 1984 in the horizontal<sup>5</sup>. The resultant grids developed from these merged spatial data sets will be sufficient to simulate wave dynamics within the inundation computation for an at-risk community.

From these digital elevation models, a set of three high-resolution, ‘reference grids’ are constructed for the development of a high-resolution ‘reference model’. On the basis of past validation and verification studies of the MOST model, many of which use a model set up similar to that described here, this reference model serves as our experimental control.

From the reference model, a further set of grids are constructed, which constitute an ‘optimized’ model. The term ‘optimized’ is used here in that these grids are constructed by sub-sampling of the reference model, in order to coarsen the resolution and shrink the overall grid dimensions. This is done with the aim that the optimized model will run significantly more quickly than the reference model and within an operationally specified period of time (usually, a 4 hour simulation of modeled tsunami waves is required to take 10 minutes or less of wall-clock time). This model will henceforth be referred to as the ‘optimized tsunami forecast model’ or ‘forecast model’ for brevity.

Table 2 provides specific details of both reference and tsunami forecast model grids, including extents. Complete input parameter information for the model runs is provided in Appendix A. The locations of the grids, including a depiction of how they are nested, are shown Figure 6

The A-grid in the reference model is identical to the grid used in the reference model developed for Portland, Maine (Spillane, 2009). This grid is relatively large, in order to contain the entire Gulf of Maine, the Georges Bank, the continental margin and outlying deep oceanic waters. It is important these coastal bathymetric features be entirely encapsulated within the grid so that shoaling of tsunamis, as they propagate from deep waters onto the continental shelf, and subsequent changes to the waveforms are well characterized.

---

<sup>5</sup> <http://ngdc.noaa.gov/mgg/inundation/tsunami/inundation.html>

The A-grid in the forecast model was designed at the same resolution, but optimized so that its southern boundary is closer to the continental margin. By moving the boundary in this manner, the deepest water depths contained within the grid are reduced, which allows a larger time-step to be used, but without inducing numerical instability<sup>6</sup>. The eastern and western boundaries were also shifted to exclude shallow waters that are not close to the area of interest (Figure 6, top-right). Coarser resolutions for the A-forecast grid were also tested with a view to further increasing the computation speed. However, these were shown to not accurately match the simulations produced by the reference model. Compared to other tsunami forecast models developed by PMEL, the A-grid in the Bar Harbor forecast model is very large. However, this is necessary since the continental shelf is very wide in the region of interest.

Given the relative complexity of the coastline in this region, the B-grid of the reference model was chosen roughly centered on Frenchman Bay and extended to encompass all coastal waters surrounding Mt Desert Island roughly 50km (31 miles) in each direction. The B-grid of the forecast model was constructed at a resolution coarser than its reference model counterpart, as well as covering a smaller area (see Figure 6 bottom right). The C-grids were chosen centered on Bar Harbor and so that the grid boundaries do not intersect any of the nearby islands of Frenchman Bay. Both grids cover the same area, but the C-forecast grid is at a coarser resolution (Figure 7).

For both models, the grids required some modification in order to obtain numerically stable solutions. These modifications included some manipulations that were required over the entirety of each grid. Algorithms that identify and reduce any regions of excessive steepness, as well as those that ‘smooth’ extremely fine-scale features were employed. Without application of these tools, such geographic features may generate numerical instabilities.

Further, fine-scale modifications were performed over localized coastal regions. This was usually achieved by manually changing the elevation of individual grid points so that they were made to be above sea level. This technique was employed to deal with grid points where instabilities were generated only in locations well away from Bar Harbor (e.g. on the B-grids or near the edge of the C-grids).

In other places, modifications were made to improve the representation of specific features, particularly in the C-forecast grid. For example, the relatively low resolution of this grid means that the breakwater extending from Bald Porcupine Island is not entirely resolved. Therefore, grid points were manually modified to make the breakwater artificially wide so that it was complete and unbroken along its length.

Another manual modification was made to the C-forecast grid in the vicinity of the tide gauge. The narrow peninsula immediately to the east of the tide gauge location was only 1-grid node in width. Also, the grid node nearest to the tide gauge location was extremely shallow (less than 1 meter in depth). The algorithm within the MOST model cannot handle such narrow geographic features and so the width of this peninsula was increased by 1 node on the eastern side (i.e. the opposite side to the tide gauge location) and the grid point closest to the tide gauge was deepened slightly. An example of the effects of these localized modifications, as well as those applied to the entire grid, can be seen in Figure 8.

---

<sup>6</sup> In this context, instability is of the type generated when the Courant-Friedrichs-Lewy condition is not met.

## 3.4. Synthetic Scenarios

The accuracy of the forecast model was tested using 8 hypothetical tsunami scenarios. These scenarios were constructed from SIFT propagation database (Gica et al., 2008) using unit sources located in the Caribbean region (shown in Figure 10) and the South Sandwich Islands region (shown in Figure 11). Parameters for the synthetic scenarios are listed in Table 3.

The first stability test of the models was to simulate a very small tsunami. A single unit source in the South Sandwich Islands region was scaled by 0.5 (equivalent to a magnitude 7.3 earthquake) and used to produce a so-called ‘micro scenario’, the location of which is indicated in Figure 11. Testing with this scenario ensures that no instability or other spurious oscillations arise in the models when they are largely unperturbed.

Six more scenarios (5 in the Caribbean, 1 in the South Sandwich Islands) were constructed by linearly combining multiple (20 in each scenario) magnitude 7.5 unit sources. The resultant combined sources form a series of mega-tsunami scenarios, each approximately equivalent to a magnitude 9.3 earthquake. These will be termed scenarios 1 to 5 (Caribbean) and scenario 6 (South Sandwich Islands). The locations of the unit sources that are combined to make each of scenarios 1 through 5 are indicated in Figure 10 while the location of scenario 6 is indicated in Figure 11. Testing with these very large magnitude scenarios ensure the models are stable under extreme forcing.

A seventh scenario was constructed from a single magnitude 7.5 unit source in the Caribbean. Though much less severe, this source tests the stability of the model using a scenario that is indicative of an earthquake in this region that has a much shorter return period than the mega-tsunami cases. The unit source used for scenario 7 is also indicated on Figure 10.

## 3.5. Historical Event Scenarios

In addition to the synthetic scenarios described above, the single historical event described in section 3.2 was also considered. The scenario used in this study to represent the tsunami generated by the Great Lisbon Earthquake is based on the rupture parameters of Barkan et al. (2009). The parameters of this source are listed in Table 4. Within the SIFT propagation database, this source has code *lila* and a map of this source is illustrated in Figure 9.

## 4.0 Results and Discussion

### 4.1. Results from the Synthetic Micro Scenario

Plots of the maximum amplitude for the forecast and reference C-grids are shown in Figure 12 and time series of sea-level elevations at the tide gauge location are shown in Figure 13. The plots show that in the absence of significant forcing, the models remain unperturbed. Figure 13 does display some very small oscillations in both time series. However they do not grow larger than approximately 1mm, providing a high degree of confidence that both models do not generate any numerical instabilities.

## 4.2. Results from Other Synthetic Scenarios

Results from the other synthetic scenarios are displayed as maximum amplitude plots and time series from Figure 14 through to Figure 27. The time series are taken from the grid node nearest the tide gauge location. Furthermore, various indices that indicate the degree of agreement have been calculated for each time series. A description of these indices is included in Appendix C and the results are included in Table 5.

All scenarios, except scenario 7, display a good agreement between the forecast and reference model and even scenario 7 still shows reasonable agreement (this is discussed in more detail below). In all cases, the forecast model captures the character of the reference model well, although it does show an overall tendency to under-predict amplitudes. The degree of under-prediction can be estimated from the values of the ‘Normalised error in the maximum amplitude’ index,  $\epsilon_{\max}$ , in Table 5. The values of  $\epsilon_{\max}$  in this table suggest under-prediction (specifically, of the maximum value) on the order of 30 – 40%. This has implications, not only for the forecast water heights, but also tsunami currents, as simulations that correctly forecast the phase of a tsunami, but underestimate its amplitude are also likely to underestimate the associated current velocities.

Perhaps the most significant scenarios are scenarios 1 and 2, since they are, by far, the largest scenarios, in terms of the amplitudes observed over the grids and at the tide gauges. These scenarios show some inundation of low-lying areas, particularly scenario 2. In these cases, the forecast model time series displays a good match to the reference model, a notion supported by the indices in Table 5. This match is best over the period of time immediately following the tsunami arrival. After approximately two hours, the models diverge slightly, as amplitudes in the forecast model begin to be under-predicted compared to the reference model (this appears to be slightly worse in scenario 1). It is important to note that in both cases, large values occur throughout the entire time series. Scenario 2, in particular, displays very large values towards the end of the calculated series. These large values likely result from waves arriving at the tide gauge following reflections from bathymetric features, both regional (that is within the inundation model grids) and remote (within the SIFT propagation database). The coarse resolution of the forecast model appears to generate less inundation of coastal areas than the reference model for scenarios 1 and 2 (a clear example of this can be seen in Figure 16 in the vicinity of the Bar Harbor township and the artificial breakwater of Bald Porcupine Island – see Figure 2).

Scenario 5 arguably shows the best agreement between the forecast and reference models among all scenarios. The time series Figure 23 show a high degree of correlation and the values of the indices in Table 5 are the second highest of all scenarios, after scenario 4. However, the fields of maximum amplitude presented in Figure 22 provide arguably the best match of all scenarios, in terms of the patterns and amplitudes. Closer examination of Figure 23 shows that the time series closely match from the time of arrival (approximately 5 hours after initialization) through the following 2.5 hours. After this time, the forecast model simulates the low-frequency variability well but has larger errors in the high-frequency oscillations. The maximum of the reference model time series occurs at the end of the displayed time series and the forecast model appears to underestimate this peak. However, in this case, the forecast model is late in predicting this peak so that the maximum of the forecast model time series occurs just beyond the time period covered by Figure 23.

The results for scenario 4 present an unusual case. The time series in Figure 21 shows the highest degree of agreement of all scenarios, and this is confirmed by the values of the

indices in Table 5. Yet unlike the other scenarios, the series are largely devoid of any high-frequency oscillations. Furthermore, the plot of maximum amplitudes in Figure 20 shows that for this scenario, the forecast model tends to over predict compared to the reference model. This behavior is unique among the scenarios considered in this report.

Scenario 6 is also unique in that it is the only case (other than the micro scenario) with sources not located in the Caribbean. It also shows some unique behavior in its time series (Figure 25). While the other ‘mega’ tsunami scenarios (1-5) show a distinct low-frequency component with periods on the time scale of hours, scenario 6 is devoid of such oscillations. Furthermore, well after the arrival of the tsunami, the high-frequency oscillations present grow appreciably. It is not clear whether this amplification is due to local dynamics around Bar Harbor or boundary forcing later in the time series (for example, due to the possible reflection of energy in the Atlantic Ocean basin). However, what is most important is that the forecast model is able to capture this behavior, with the indices indicating a level of agreement as high as the other scenarios. Like the other scenarios, the time series (Figure 25) shows that the forecast model tends to slightly under-predict the reference model and this behavior is also very apparent in the fields of maximum amplitude (Figure 24).

The smallest scenario considered here, scenario 7, is the scenario where the forecast model most poorly reproduces the reference model. As in all other scenarios, there is initially good agreement between time series of the models (Figure 27), but after approximately 1 hour, they begin to diverge. Initially, the amplitudes of the forecast model decrease, while there is some growth in the reference model. However, later into the series, the oscillations also become out of phase. Table 5 also shows that the forecast model does a relatively poorly at simulating the reference model with the lowest scores for all indices. Likewise, the plots of maximum amplitude show notable differences (Figure 26). This case is instructive as it demonstrates how even in the absence of significant forcing (as in, overall variations are small, compared to other scenarios), the interactions at the coast are relatively important.

### **4.3. Results from the Historical Event Scenario**

As described above, the only historical event considered in this report is the 1755 Great Lisbon Earthquake. Since there are no sea-level or other observations of the event from the Bar Harbor region, the event can only be evaluated in the same manner as the synthetic scenarios, that is, by comparison of the reference and forecast models. As described in section 3.5, A source for this event exists in the SIFT database and the results from this source are shown in the same way as for the synthetic scenarios, That is, by comparing plots of maximum amplitude (Figure 28) as well as time series taken from the grid nodes nearest the tide gauge location (Figure 29).

As for the synthetic scenario, there is good agreement between the reference and forecast models. By considering Figure 29, it can be seen the models match in their predictions of the arrival, phase and magnitude of the earliest waves. However, as for the synthetic scenarios, after the first few initial wavelengths, the models diverges. At first, the forecast model begins to under-predict the amplitudes of the reference model, while retaining a high correlation with the reference model’s oscillations. After approximately 6 hours after arrival, this correlation begins to weaken somewhat.

As for the synthetic scenarios, the degree of under-prediction can be roughly quantified by considering the  $\varepsilon_{\max}$  index in Table 5, which shows underestimation of the maximum value by approximately 35%.

The underestimation of amplitudes in the forecast model, compared to the reference model is also clear when comparing the spatial plots of maximum amplitude for the forecast and reference models (Figure 28). This figure suggests a similar degree of under-prediction as the time-series. However, it should also be noted that the spatial patterns do show a good correspondence, with the largest values for both grids found in the Eddie Brook outflow and Hulls Cove regions (see Figure 2).

## 4.4. Discussion

There are some consistent features among the scenarios. The time series plots show that despite its differences from the reference model, the forecast model simulates the arrival time of tsunamis at the Bar Harbor tide gauge location well. The initial waves following arrival match well and the model also retains the low-frequency character of the reference model. However, high-frequency oscillations begin to be attenuated after 1-4 hours. It is suggested that this is the reason that the forecast model also tends to underestimate the peak amplitude of the reference model (a feature not only apparent the times series, but also in the maximum amplitude plots). Further experimentation with the forecast model grids suggest this is primarily due to the coarser resolution of the B- and C-grids. For example, some effort was required to maintain in inclusion of the Bald Porcupine Island artificial breakwater (see Figure 2 and Figure 8). However, the reduced spatial extent of the A- and B-grids is a secondary contributing factor.

Another key feature of tsunami behavior in the Bar Harbor region is the persistence of tsunami energy, as revealed by the time series. All cases show oscillations that persist throughout the time series. In some, specifically, scenarios 2, 4, 5 and 6, very large values (sometimes the maximum) occur well after arrival. This may result from local interactions, but it is more likely to arise from waves arriving at Bar Harbor following reflections from regional (i.e. within the outer model grids) or even distant bathymetric features (such as the African coastline). This characteristic is important for warning guidance, as dangerous conditions may persist for many hours following arrival of the initial tsunami.

The maximum amplitude plots for scenario 1 and 2 (Figure 14 and Figure 16 respectively) do show patterns, by way of large sea level amplitudes and inundation, that suggest the regions surrounding Bar Harbor where tsunami impact may be greatest. These at-risk regions, indicated in Figure 2, include the shallow channel and sand bar between Bar Harbor and Bar Island, the region at the mouth of Eddie Brook, Hulls Cove and Cromwell Cove. Some other coves to the south of Cromwell Cove would also experience impact. Of these areas, the Eddie Brook region and Hulls Cove would experience the greatest impact, with the largest values for smaller scenarios such as scenarios 6 and 7, being observed in the maximum amplitude plots in these regions.

It was mentioned in section 3.3 that the forecast model should be designed to run within a operationally specified period of time, specifically 4 hours of simulation should be completed within 10 minutes of wall-clock time. Table 2 states that the forecast model for Bar Harbor does not run within this time, but instead completes 4 hours of tsunami simulation in 21 minutes. Tests show that this relatively slow speed is due to the large forecast A-grid, which is required to adequately simulate the transmission of tsunamis onto the very wide continental shelf present in this region. However, it should be noted that the speed of the Bar Harbor Forecast model is similar to other models developed for the Atlantic Basin for use with SIFT (e.g. Wei, 2010). Moreover, Bar Harbor's distant proximity from

potential tsunamigenic sources means that forecast model's speed is still sufficient to complete a simulation for use in supplying forecast and warning guidance.

## 5.0 Summary and Conclusions

This report outlines the steps take to generate a tsunami forecast model for Bar Harbor, Maine. An outline of the steps taken to produce the bathymetric grids was provided. In the absence of any historical records of past tsunami events in the Atlantic basin, the resulting model was tested using a series of synthetic scenarios.

The scenarios revealed that the low-resolution forecast model performs well at reproducing the characteristics simulated in the high-resolution reference model. Although it consistently matches the character of the high-resolution model, it tends to under-predict the amplitude of the reference model. This implies that the forecast model is predisposed to underestimating the potential impacts in the regions of interest (from a forecast perspective).

These issues may be alleviated by future revisions of the forecast model. As computing power increases and model technology improves, the resolution of the forecast grids may be increased, while still maintaining computation speeds that are within or reasonably close to the target run-time. Increasing the spatial extent of the grids may also improve the forecast model's accuracy.

## 6.0 Acknowledgments

Assistance with the development of this model was gratefully received from Diego Arcas, Yong Wei, Edison Gica, Christopher Moore, Mick Spillane, Elena Tolkova and Marie Eble.

The image used for Figure 4 was accessed from Flickr.com and is attributed to user *Smudge 9000*. It used under the Creative Commons Attribution 2.0. Figure 3 was taken from Google Earth.

This publication is partially funded by the Joint Institute for the study of the Atmosphere and Ocean (JISAO) under NOAA Cooperative Agreement No. NA17RJ1232, JISAO Contribution No. XXXX. This is PMEL Contribution No. NNNN

Funding source – NOAA & JISAO will be added to each report

JISAO & PMEL publication #'s will be provided

## 7.0 References

Allen, S.C.R and D.J.M. Greenslade (2012): Indices for the Objective Assessment of Tsunami Forecast Models. *Pure Appl. Geophys.*, 170(9–10), pp 1601–1620, doi: 10.1007/s00024-012-0522-4

Barkin, R. U.S. ten Brink and J. Lin (2009): Far field tsunami simulations of the 1755 Lisbon earthquake: Implications for tsunami hazard to the U.S. East Coast and the Caribbean. *Mar. Geol.* 264(1–2), 109–122, doi:10.1016/j.margeo.2008.10.010

- Gica, E., M. Spillane, V.V. Titov, C. Chamberlin, and J.C. Newman (2008): Development of the forecast propagation database for NOAA's Short-term Inundation Forecast for Tsunamis (SIFT). NOAA Tech. Memo. OAR PMEL-139, 89 pp.
- Gutscher, M.-A., M.A. Baptista and J.M. Miranda (2006): The Gibraltar Arc seismogenic zone (part 2): Constraints on a shallow east dipping fault plane source for the 1755 Lisbon earthquake provided by tsunami modeling and seismic intensity. *Technophys.*, 426(1–2), 153–166, doi:10.1016/j.tecto.2006.02.025.
- Mielke, P.W., Jr. (1984): Meteorological applications of permutation techniques based on distance functions. In Krishnaiah, P.R. and Sen, P. K. (eds.), *Handbook of Statistics*, Vol 4, Elsevier, Amsterdam, 813-830.
- Mielke, P.W., Jr. and Berry, K.J. (2001): *Permutation Methods: A Distance Function Approach*. Springer-Verlag, New York, 352pp.
- Spillane, M.C. (2009): Development of a Tsunami Forecast Model for Portland, Maine. NOAA OAR Special Report, PMEL Tsunami Forecast Series: Vol. NNNN, MMMM pp.
- Synolakis, C.E., E.N. Bernard, V.V. Titov, U. Kânoğlu, and F.I. González (2008): Validation and verification of tsunami numerical models. *Pure Appl. Geophys.*, 165(11–12), 2197–2228.
- Tang, L., V.V. Titov, Y. Wei, H.O. Mofjeld, M. Spillane, D. Arcas, E.N. Bernard, C. Chamberlin, E. Gica, and J. Newman (2008): Tsunami forecast analysis for the May 2006 Tonga tsunami. *J. Geophys. Res.*, 113, C12015, doi: 10.1029/2008JC004922.
- Tang, L., V. V. Titov, and C. D. Chamberlin (2009): Development, testing, and applications of site-specific tsunami inundation models for real-time forecasting, *J. Geophys. Res.*, 114, C12025, doi:10.1029/2009JC005476.
- Titov, V., and F.I. González (1997): Implementation and testing of the Method of Splitting Tsunami (MOST) model. NOAA Tech. Memo. ERL PMEL-112 (PB98-122773), NOAA/Pacific Marine Environmental Laboratory, Seattle, WA, 11 pp.
- Titov, V.V., F.I. González, E.N. Bernard, M.C. Eble, H.O. Mofjeld, J.C. Newman, and A.J. Venturato (2005): Real-time tsunami forecasting: Challenges and solutions. *Nat. Hazards*, 35(1), Special Issue, U.S. National Tsunami Hazard Mitigation Program, 41–58.
- Titov, V.V. (2009): Tsunami forecasting. Chapter 12 in *The Sea*, Volume 15: Tsunamis, Harvard University Press, Cambridge, MA and London, England, 371–400.
- Watterson, I.G. (1996): Non-dimensional measures of climate model performance. *Int. J. Climatol.*, 16, 379–391.
- Wei, Y., E. Bernard, L. Tang, R. Weiss, V. Titov, C. Moore, M. Spillane, M. Hopkins, and U. Kânoğlu (2008): Real-time experimental forecast of the Peruvian tsunami of August 2007 for U.S. coastlines. *Geophys. Res. Lett.*, 35, L04609, doi: 10.1029/2007GL032250.
- Wei, Y. (2010): Development Of A Tsunami Forecast Model For Ocean City, Maryland. NOAA OAR Special Report, PMEL Tsunami Forecast Series: Vol. NNNN, MMMM pp.
- Willmott, C.J. (1981): On the validation of models. *Phys. Geogr.*, 2, 184–194.

Willmott, C.J., Ackleson, S.G., Davis, R.E., Feddema, J.J., Klink K.M., Legates, D.R., O'Donnell, J. and Rowe, C.M. (1985): Statistics for the evaluation of model performance. *J. Geophys. Res.*, 90(C5), 8995–9005.

# Tables

Table 1: Tidal characteristics for the Bar Harbor tide gauge. Data taken from <http://tidesandcurrents.noaa.gov/geo.shtml?location=8413320>.

Table 2: MOST setup parameters for reference and forecast models for Bar Harbor, Maine.

Table 3: Synthetic tsunami events. The locations of the sources are shown in Figure 10 and Figure 11.

Table 4: Source Parameters used for the Great Lisbon Earthquake source (after Barkan et al., 2009).

Table 5: Values of various indices for each of the seven synthetic scenarios considered and the micro synthetic scenario. A description of the indices is given in Appendix C.

# Figures

Figure 1: Contour relief of the Gulf of Maine. The features labeled are (a) the Gulf of Maine, (b) The Georges Bank, (c) The Northeast Channel, (d) The Great South Channel, (e) Cape Cod and (f) Cape Sable Island (approx.). These features are referenced in the text. The approximate location of Bar Harbor is indicated by the red cross. Depths are in meters.

Figure 2: Contour relief of Frenchman bay. Units are in meters. The features labeled are (a) Bar Harbor township, (b) Long Porcupine Island, (c) Burnt Porcupine Island (d) Sheep Porcupine Island, (e) Bar Island, (f) Bald Porcupine Island (Note the breakwater extending east.), (g) Cromwell Cove (h) outflow region from Eddie Brook and (i) Hulls Cove. These features are referenced in the text. The location of the tide gauge is indicated by the red cross and depths are in meters.

Figure 3: Aerial photography of the Bar Harbor region. Key land features are labeled. Taken from Google Earth.

Figure 4: Oblique aerial view of the Bar Harbor region. Photograph by Flickr user Smudge 9000, used under Creative Commons Attribution 2.0.

Figure 5: Instrument housing for the Bar Harbor tide gauge.

Figure 6: A depiction of the extent and location of the forecast grids, including how each is nested. The top-left figure shows the extent of the A reference grid. The top-right figure shows this grid in more detail with the extent of the A forecast grid shown by the yellow rectangle and the extent of the B reference grid shown by the red rectangle. The other figures following a similar manner. Note that there is no yellow rectangle depicting the extent of the C forecast grid, since it covers the same areas as the C reference grid.

Figure 7: Comparison of the C reference grid (left) with the C forecast grid. Depths are in meters.

Figure 8: An example of some of the effects of necessary bathy modifications on the C forecast grid in the vicinity of Bar Harbor (the unmodified bathymetry is shown on the left). Note the changes to the breakwater and the area near the tide gauge (marked by the red cross). The effects of smoothing over the entire grid are also apparent on the form of the (underwater) contours.

Figure 9: Location of the source used to represent the tsunami generated by the 1755 Great Lisbon Earthquake.

Figure 10: Location of Caribbean unit sources. The synthetic scenarios used in this study consist of scaling and combining these unit sources. The unit sources that make up each scenario are colored according to the key. The single unit source that comprises scenario 7 is also used by scenario 2.

Figure 11: Location of the South Sandwich Sources. As in Figure 10, the unit sources that make up each scenario are colored according to the key.

Figure 12: Plot of maximum amplitude for both the forecast and reference C grids for the micro scenario. Units are in cm and the location of the tide gauge is shown by the magenta cross.

Figure 13: Time series of sea-level elevations at the forecast and reference grid nodes nearest the Bar Harbor tide gauge for the micro scenario. The series from the forecast grid is shown in red and the series for the reference model is shown in

black. Units are in cm. The length of both series is 12 hours, calculated from when the tsunami first reaches the edge of the respective A grids.

Figure 14: Plot of maximum amplitude for both the forecast and reference C grids for scenario 1. Units are in cm and the location of the tide gauge is shown by the magenta cross.

Figure 15: Time series of sea-level elevations at the forecast and reference grid nodes nearest the Bar Harbor tide gauge for scenario 1. The series from the forecast grid is shown in red and the series for the reference model is shown in black. Units are in cm.

Figure 16: Plot of maximum amplitude for both the forecast and reference C grids for scenario 2. Units are in cm and the location of the tide gauge is shown by the magenta cross.

Figure 17: Time series of sea-level elevations at the forecast and reference grid nodes nearest the Bar Harbor tide gauge for scenario 2. The series from the forecast grid is shown in red and the series for the reference model is shown in black. Units are in cm.

Figure 18: Plot of maximum amplitude for both the forecast and reference C grids for scenario 3. Units are in cm and the location of the tide gauge is shown by the magenta cross.

Figure 19: Time series of sea-level elevations at the forecast and reference grid nodes nearest the Bar Harbor tide gauge for scenario 3. The series from the forecast grid is shown in red and the series for the reference model is shown in black. Units are in cm.

Figure 20: Plot of maximum amplitude for both the forecast and reference C grids for scenario 4. Units are in cm and the location of the tide gauge is shown by the magenta cross.

Figure 21: Time series of sea-level elevations at the forecast and reference grid nodes nearest the Bar Harbor tide gauge for scenario 4. The series from the forecast grid is shown in red and the series for the reference model is shown in black. Units are in cm.

Figure 22: Plot of maximum amplitude for both the forecast and reference C grids for scenario 5. Units are in cm and the location of the tide gauge is shown by the magenta cross.

Figure 23: Time series of sea-level elevations at the forecast and reference grid nodes nearest the Bar Harbor tide gauge for scenario 5. The series from the forecast grid is shown in red and the series for the reference model is shown in black. Units are in cm.

Figure 24: Plot of maximum amplitude for both the forecast and reference C grids for scenario 6. Units are in cm and the location of the tide gauge is shown by the magenta cross.

Figure 25: Time series of sea-level elevations at the forecast and reference grid nodes nearest the Bar Harbor tide gauge for scenario 6. The series from the forecast grid is shown in red and the series for the reference model is shown in black. Units are in cm.

Figure 26: Plot of maximum amplitude for both the forecast and reference C grids for scenario 7. Units are in cm and the location of the tide gauge is shown by the magenta cross.

Figure 27: Time series of sea-level elevations at the forecast and reference grid nodes nearest the Bar Harbor tide gauge for scenario 7. The series from the forecast grid is shown in red and the series for the reference model is shown in black. Units are in cm.

Figure 28: Plot of maximum amplitude for both the forecast and reference C grids for the SIFT database source *li1a*, used to represent the tsunami generated by the 1755 Great Lisbon Earthquake. Units are in cm and the location of the tide gauge is shown by the magenta cross.

Figure 29: Time series of sea-level elevations at the forecast and reference grid nodes nearest the Bar Harbor tide gauge for the SIFT database source *li1a*, used to represent the tsunami generated by the 1755 Great Lisbon Earthquake. The series from the forecast grid is shown in red and the series for the reference model is shown in black. Units are in cm.

## Appendix A

Development of the Bar Harbor, Maine tsunami forecast model occurred prior to parameter changes that were made to reflect modifications to the MOST model code. As a result, the input file for running both the optimized tsunami forecast model and the high-resolution reference inundation model in MOST have been updated accordingly. Appendix A1 and A2 provide the updated files for Bar Harbor, Maine.

### A.1 Reference model \*.in file

```
0.0001      Minimum amplitude of input offshore wave (m)
5.0        Input minimum depth for offshore (m)
0.1        Input "dry land" depth for inundation (m)
0.0009      Input friction coefficient (n**2)
1          A & B-grid runup flag (0=disallow, 1=allow runup)
100.0      Blow-up limit (maximum eta before blow-up)
0.25       Input time step (sec)
172800     Input number of steps
8          Compute "A" arrays every nth time step, n=
4          Compute "B" arrays every nth time step, n=
120        Input number of steps between snapshots
1          ...Starting from
1          ...Saving grid every nth node, n=1
```

### A.2 Forecast Model \*.in file

```
0.0001      Minimum amplitude of input offshore wave (m)
5.0        Input minimum depth for offshore (m)
0.1        Input "dry land" depth for inundation (m)
0.0009      Input friction coefficient (n**2)
1          A & B-grid runup flag (0=disallow, 1=allow runup)
100.0      Blow-up limit (maximum eta before blow-up)
1.0        Input time step (sec)
43200     Input number of steps
3          Compute "A" arrays every nth time step, n=
6          Compute "B" arrays every nth time step, n=
30        Input number of steps between snapshots
1          ...Starting from
1          ...Saving grid every nth node, n=1
```

## **Appendix B**

Propagation data base – already generated; will be added to each report

## Appendix C Description of Indices

This report makes use of six indices to estimate the degree of agreement between the reference and forecast model. The suitability of these indices for the objective assessment of tsunami models was investigated by Allen and Greenslade (2012).

In formulating the indices, we take a series of form the reference model denoted  $R$ , which consists of  $n$  time-ordered elements  $\{R_1, R_2, \dots, R_n\}$ . We take an equivalent time series form the forecast model, which we denote  $F$  and that we wish to test against  $R$ . The series  $F$  will also consist of  $n$  time-ordered elements  $\{F_1, F_2, \dots, F_n\}$  such that each element in  $F$  corresponds, with respect to time, to an element in  $R$ . Both of these series start from some time that is defined here to be when either of the two series first exceeds a threshold of 1cm (except for the micro scenario and scenario 7, where this threshold is set to 0.1 cm).

### C.1 Normalised error in the maximum amplitude

In forecast and warning applications, knowledge of the largest expected wave is often sought. In that regard, we would seek to minimise errors in the maximum (positive) forecast amplitude. This index,  $\varepsilon_{\max}$ , is made non-dimensional by normalising by the observed maximum amplitude:

$$\varepsilon_{\max} = \frac{F_{\max} - R_{\max}}{R_{\max}}$$

where  $R_{\max}$  is the maximum value of the reference model time series, and similarly,  $F_{\max}$  is the maximum value of the forecast model time series. This index has no upper bound, but has a lower bound of -1 when  $R_{\max}$  is much larger than  $F_{\max}$  and under the reasonable assumption that both  $R_{\max}$  and  $F_{\max}$  are both positive. A perfect estimation by the forecast model of the maximum amplitude is indicated by a value of zero. Given this, over- or under-prediction of the reference model maximum value is denoted by positive and negative values, respectively.

### C.2 Pearson correlation coefficient

The Pearson correlation coefficient,  $r$ , is a measure that is widely used to reveal relationships between two time series. Given the mean and standard deviations of the observed series,  $\bar{R}$  and  $\sigma_R$  respectively, and the same for the predicted series,  $\bar{F}$  and  $\sigma_F$ , the coefficient is calculated for a time series of  $n$ -elements in length by

$$r = \frac{1}{n-1} \sum_{i=1}^n \frac{(F_i - \bar{F})}{\sigma_F} \frac{(R_i - \bar{R})}{\sigma_R}$$

The coefficient is bounded over  $[-1, 1]$ , with 1 indicating a perfect linear relationship between the forecast and reference model time series, and -1 indicating a perfect, but inverse linear relationship. It should be noted that this index does not take into account differences in variance between the two series.

### C.3 Normalised Root-mean-square error

The root-mean-square error, RMSE, is another common index used to assess model performance. It is essentially a measure of the mean deviation of the forecast model time series from the reference model time series. Normalised RMSE used here is:

$$\text{nRMSE} = \frac{1}{\sigma_R} \sqrt{\frac{1}{n} \sum_{i=1}^n (F_i - R_i)^2}$$

Values of RMSE have a minimum value of 0, indicating perfect agreement (or zero error), but no upper bound.

### C.4 Index of Agreement

Willmot (1981) devised a complementary index to RMSE that aims to specify “the degree to which the observed (i.e. reference model time series) deviations about  $\bar{R}$  correspond, both in magnitude and sign, to the predicted (forecast) deviations about  $\bar{R}$ ” (Willmot, 1981). Following further refinements by Willmot et al. (1985), this Index of Agreement, IOA, is formulated as:

$$\text{IOA} = 1 - \frac{\sum_{i=1}^n |F_i - R_i|}{\sum_{i=1}^n (|F_i - \bar{R}| + |R_i - \bar{R}|)}$$

Willmot (1981) described this ratio as being a comparison between the mean absolute deviation and the mean potential error. The values of this index are bounded between 0 and 1, with 1 indicating perfect agreement between the forecast and reference models.

### C.5 Watterson’s transformed Mielke index

Watterson (1996) made a geometric argument to transform an index by Mielke (1984) (similar to the Mielke and Berry (2001) index below). His adaption means the index is bounded over  $[-1,1]$ , with perfect agreement again indicated by a value of 1. It is formulated by:

$$M = \frac{2}{\pi} \sin^{-1} \left( 1 - \frac{\text{MSE}}{\sigma_F^2 + \sigma_R^2 + (\bar{F} - \bar{R})^2} \right)$$

where

$$\text{MSE} = \frac{1}{n} \sum_{i=1}^n (F_i - R_i)^2$$

is the mean square error.

## C.6 Mielke and Berry index

The index of Mielke and Berry (2001) is more accurately described as the Multiresponse Randomized Block Procedure (MRBP). It compares the mean absolute deviation to a measure comprised of the sum of the permutations of the deviation of each prediction from each observation.

$$\mathfrak{R} = 1 - \frac{\frac{1}{n} \sum_{i=1}^n |F_i - R_i|}{\frac{1}{n^2} \sum_{i=1}^n \sum_{j=1}^n |F_j - R_i|}$$

Predictions that are in perfect agreement with the observations give this index an upper bound of 1. Mielke and Berry (2001) state that for  $n > 2$ , this index has a lower bound of -0.5.

Table 1: Tidal characteristics for the Bar Harbor tide gauge. Data taken from <http://tidesandcurrents.noaa.gov/geo.shtml?location=8413320>.

<b>Bar Harbor, ME</b>	<b>Station ID: 8413320/ATGM1</b>	<b>44° 23' 30"N, 68° 12' 18"W 44.3917°N, 68.2050°W</b>	
<b>Tidal Datum and Range Values (Epoch 1983 – 2001)</b>			
Mean Higher-High Water	4.524 m	Diurnal Range 3.466 m	Mean Range 3.220 m
Mean High Water	4.394 m		
Mean Sea Level	2.786 m		
Mean Low Water	1.174 m		
Mean Lower-Low water	1.058 m		
<b>Nearest corresponding model grid nodes</b>			
	<b>Depth at node</b>	<b>Node coordinates</b>	<b>Node index</b>
Forecast model	2.03 m	44.3916°N, 68.2050°W	(88,72)
Reference model	3.22 m	44.3917°N, 68.2050°W	(262,213)

Table 2: MOST setup parameters for reference and forecast models for Bar Harbor, Maine.

Reference Model						Forecast Model				
Grid	Region	Coverage Lat. [°N] Lon. [°W]	Cell Size ["]	$nx \times ny$	Time Step [sec]	Coverage Lat. [°N] Lon. [°W]	Cell Size ["]	$nx \times ny$	Time Step [sec]	
A	Gulf of Maine	37.0 – 46.25 288.0 – 297.0	30	$1081 \times 1111$	2	39.3583 – 45.167 289.267 – 294.617	30	$643 \times 698$	6.0	
B	Mt Desert Island and surrounds	43.9 – 44.63 291.31 – 292.2	3	$1069 \times 877$	1	43.9525 – 44.53 291.4867 – 292.19767	$9 \times 12$	$148 \times 232$	3.0	
C	Bar Harbor/ Frenchman Bay	44.33507 – 44.431 291.7467 – 291.8500	$\frac{2}{3}$	$559 \times 517$	0.25	44.3354 – 44.431 291.7467 – 291.85	2	$186 \times 173$	1	
Minimum offshore depth [m]:			5				5			
Water depth for dry land [m]:			0.1				0.1			
Friction coefficient [ $n^2$ ]:			0.009				0.009			
CPU time for 4-hr simulation:			269 min				21 min			

Computations were performed on a single core of a Dell PowerEdge R510 containing dual Intel Xeon hex-core X5670 processors running at 2.93 GHz.

Table 3: Synthetic tsunami events. The locations of the sources are shown in Figure 10 and Figure 11.

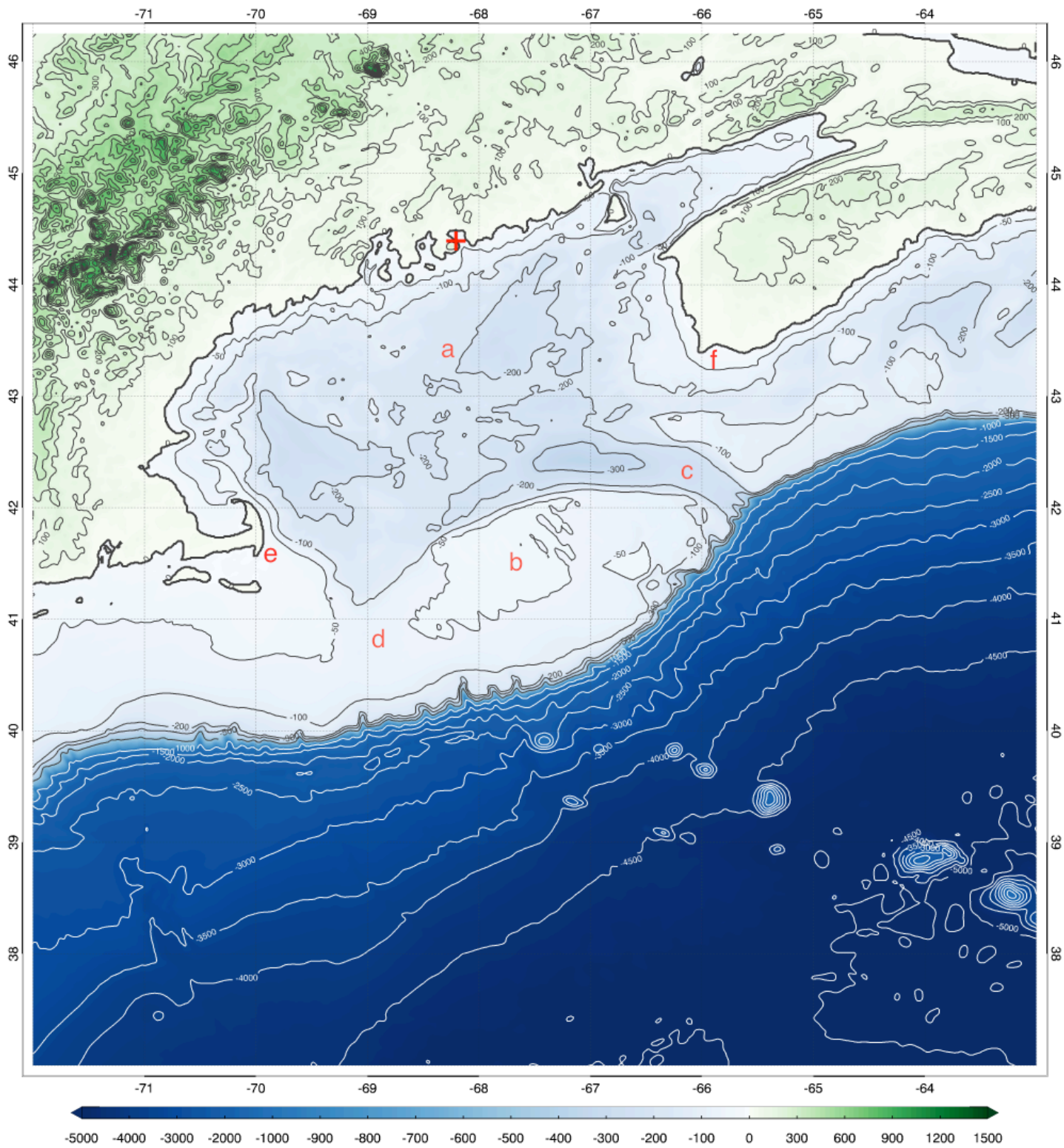
<b>Source. Number</b>	<b>Source Zone</b>	<b>Tsunami Database Unit Source(s)</b>	<b>Scale factor</b>	<b>Equivalent <math>M_w</math></b>
<b>Micro</b>	South Sandwich	B11	0.01	6.2
<b>1</b>	Atlantic	A38-A47, A38-A47	25	9.3
<b>2</b>	Atlantic	A48-A57, B48-B57	25	9.3
<b>3</b>	Atlantic	A58-A67, B58-B67	25	9.3
<b>4</b>	Atlantic	A68-A77, B68-B77	25	9.3
<b>5</b>	Atlantic	A82-A91, B82-B91	25	9.3
<b>6</b>	South Sandwich	A1-A10, B1-B10	25	9.3
<b>7</b>	Atlantic	B52	1	7.5

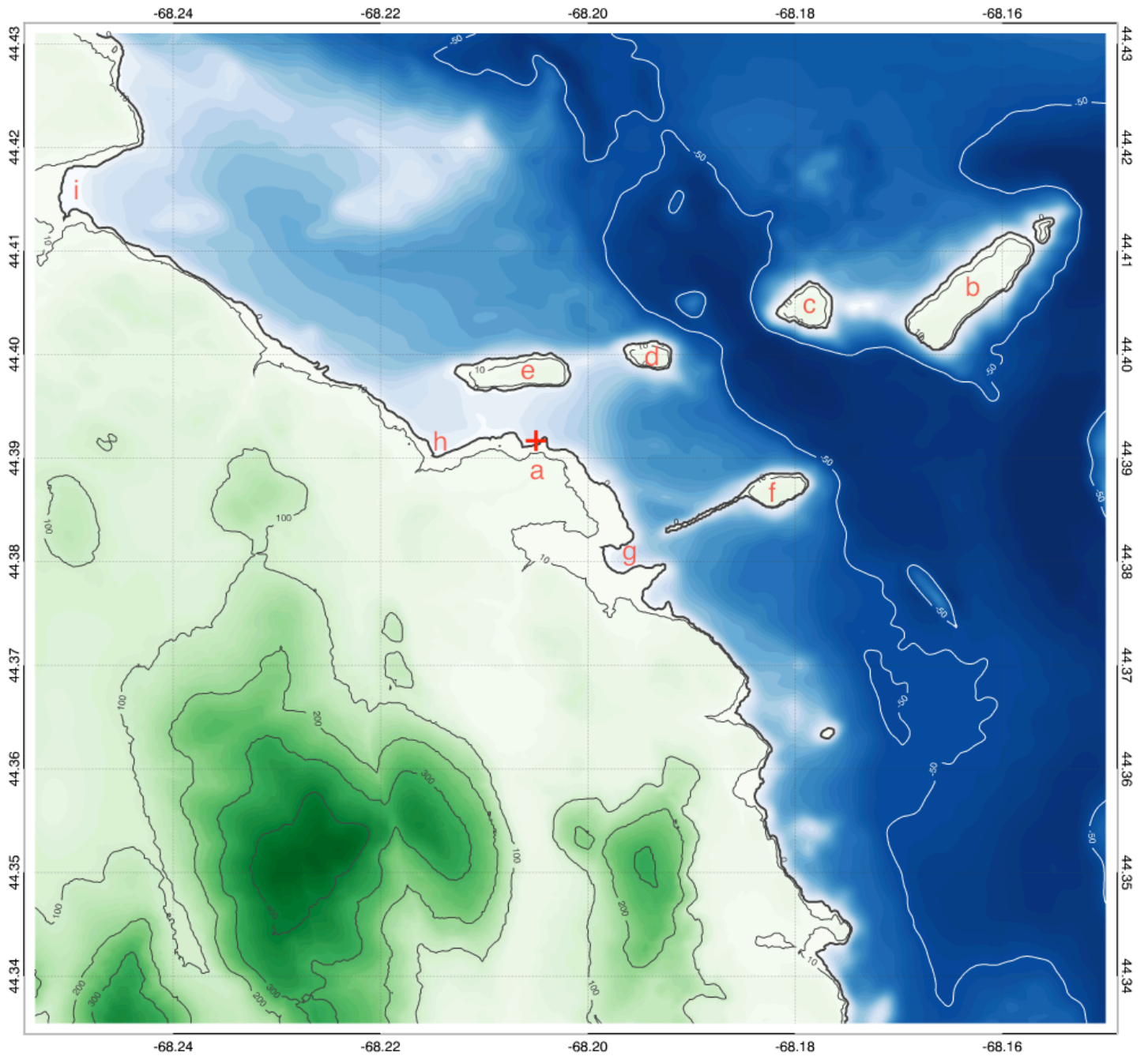
Table 4: Source parameters for the 1755 Lisbon Earthquake Source (after Barkan et al., 2009).

Source depth (km)	5
Fault length (km)	200
Fault width (km)	80
slip (m)	12.9
Dip (deg)	40
Rake (deg)	90

Table 5: Values of various indices for each of the seven synthetic scenarios considered and the micro synthetic scenario. A description of the indices is given in Appendix C.

<b>Scenario Number</b>	$\epsilon_{\max}$	$r$	nRMSE	IOA	$M$	$\mathfrak{R}$
<b>micro</b>	-0.412	0.635	0.773	0.562	0.401	0.403
<b>1</b>	-0.291	0.703	0.711	0.582	0.459	0.439
<b>2</b>	-0.368	0.723	0.692	0.642	0.494	0.542
<b>3</b>	-0.307	0.853	0.522	0.727	0.639	0.621
<b>4</b>	-0.090	0.992	0.146	0.930	0.903	0.905
<b>5</b>	-0.351	0.970	0.301	0.846	0.787	0.771
<b>6</b>	-0.377	0.753	0.665	0.637	0.487	0.506
<b>7</b>	-0.418	0.369	0.940	0.367	0.195	0.167
<b>Lisbon 1755</b>	-0.349	0.763	0.655	0.621	0.494	0.473

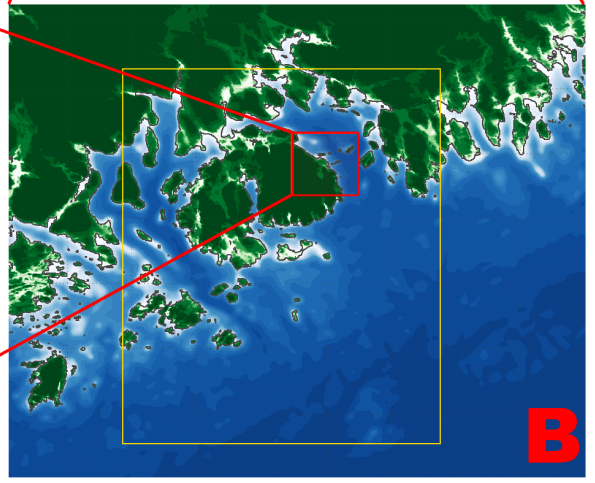
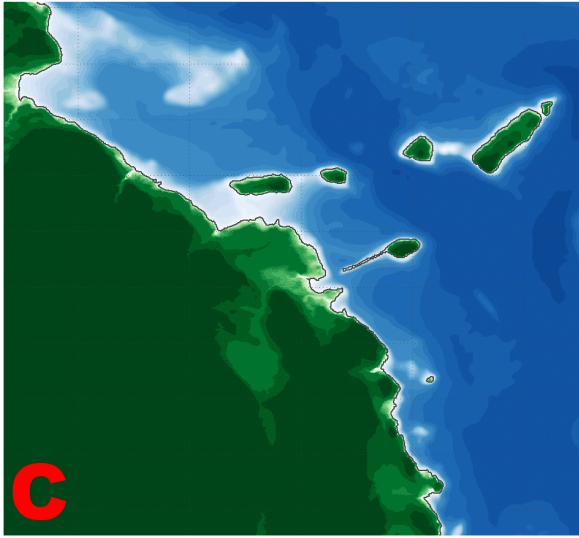
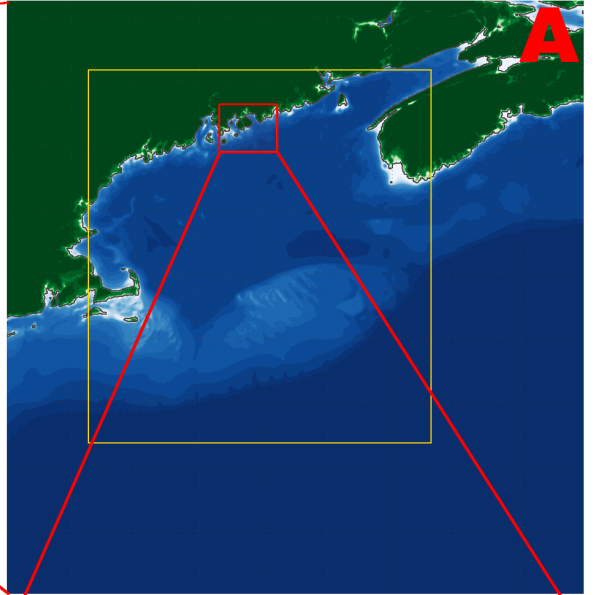
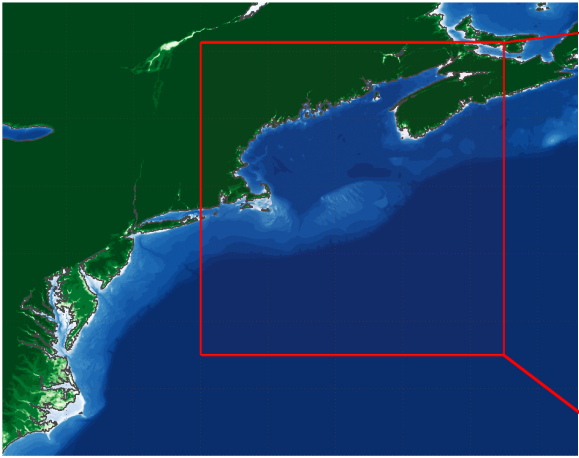


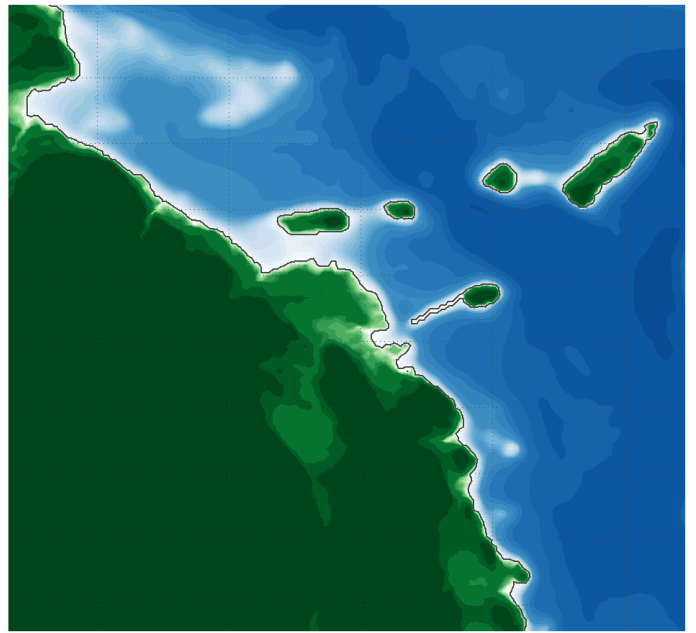
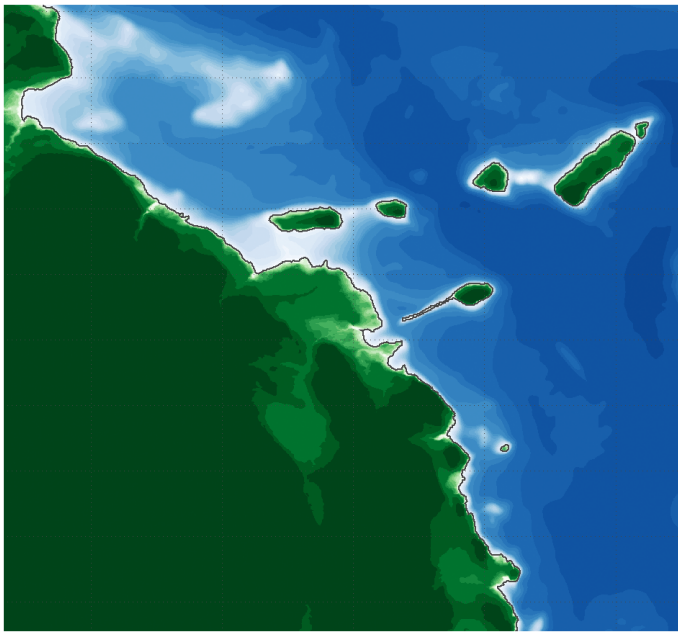


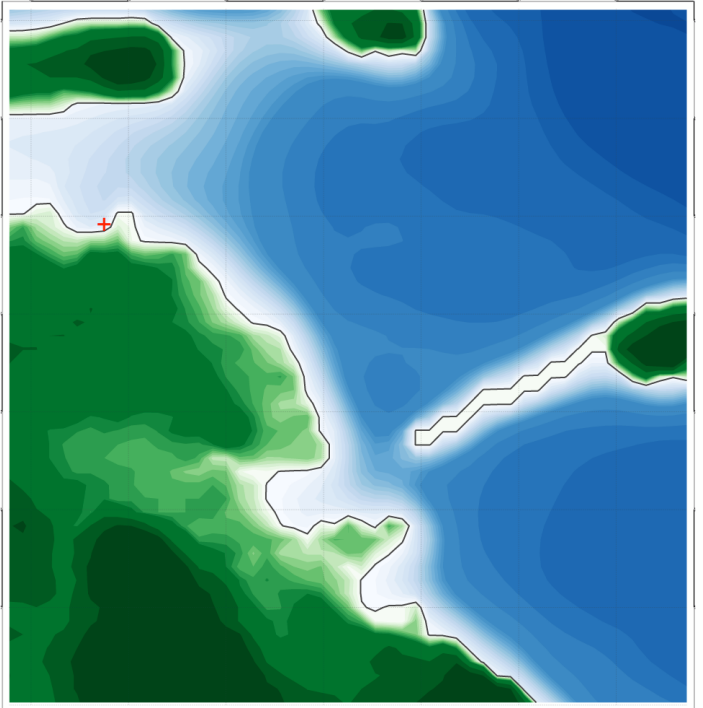
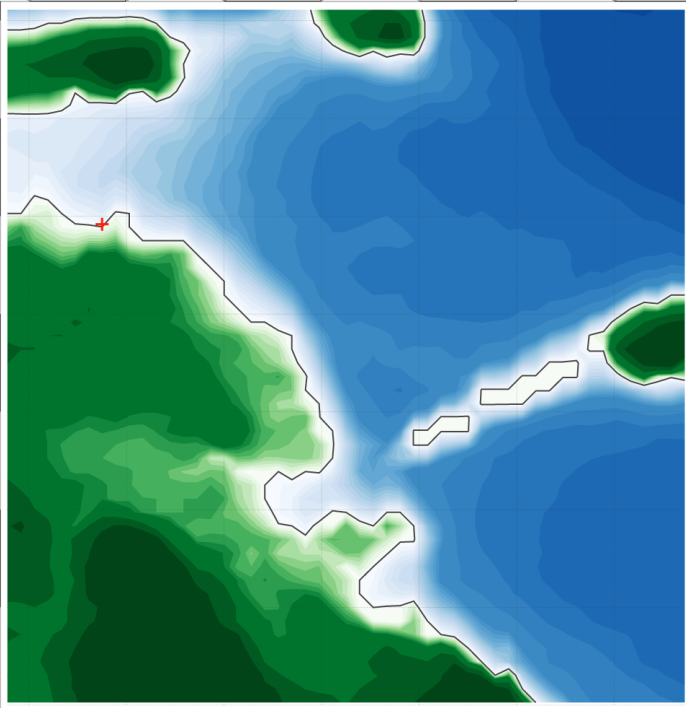


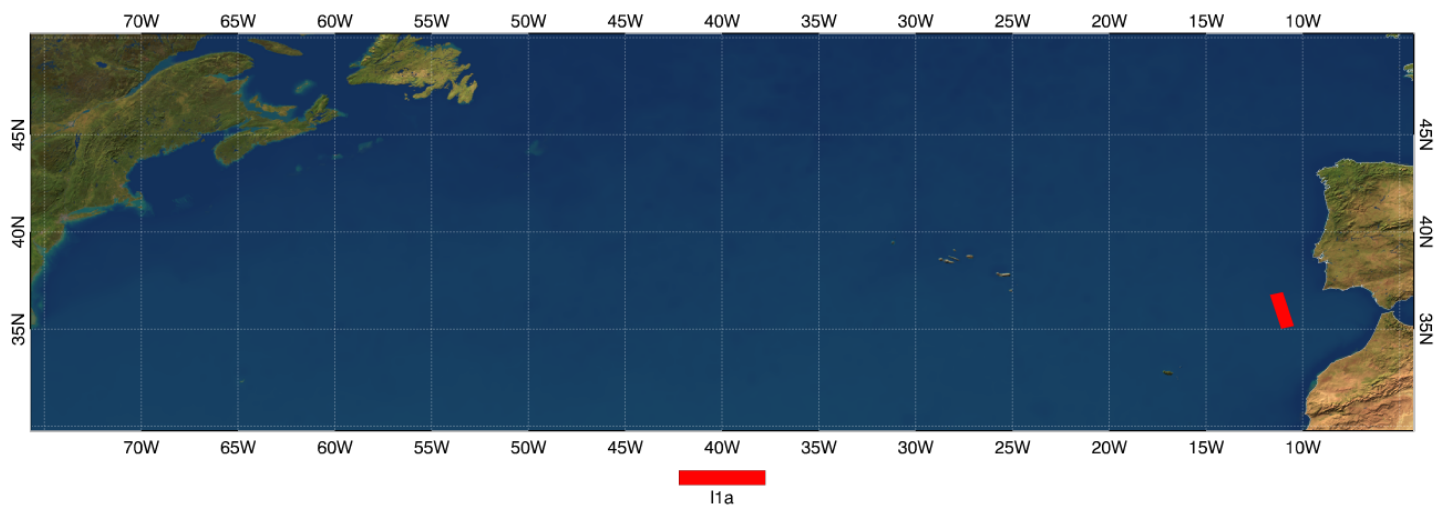


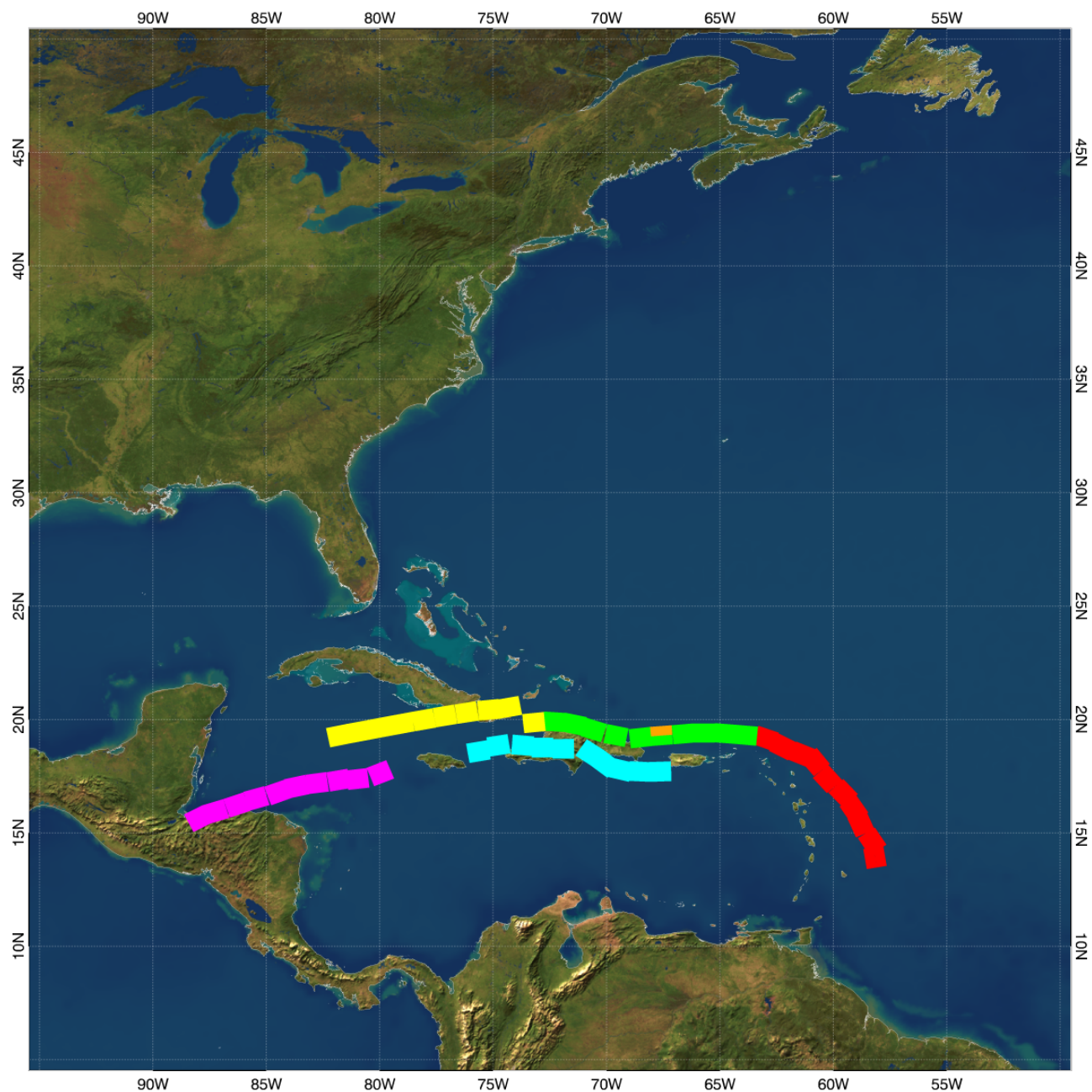


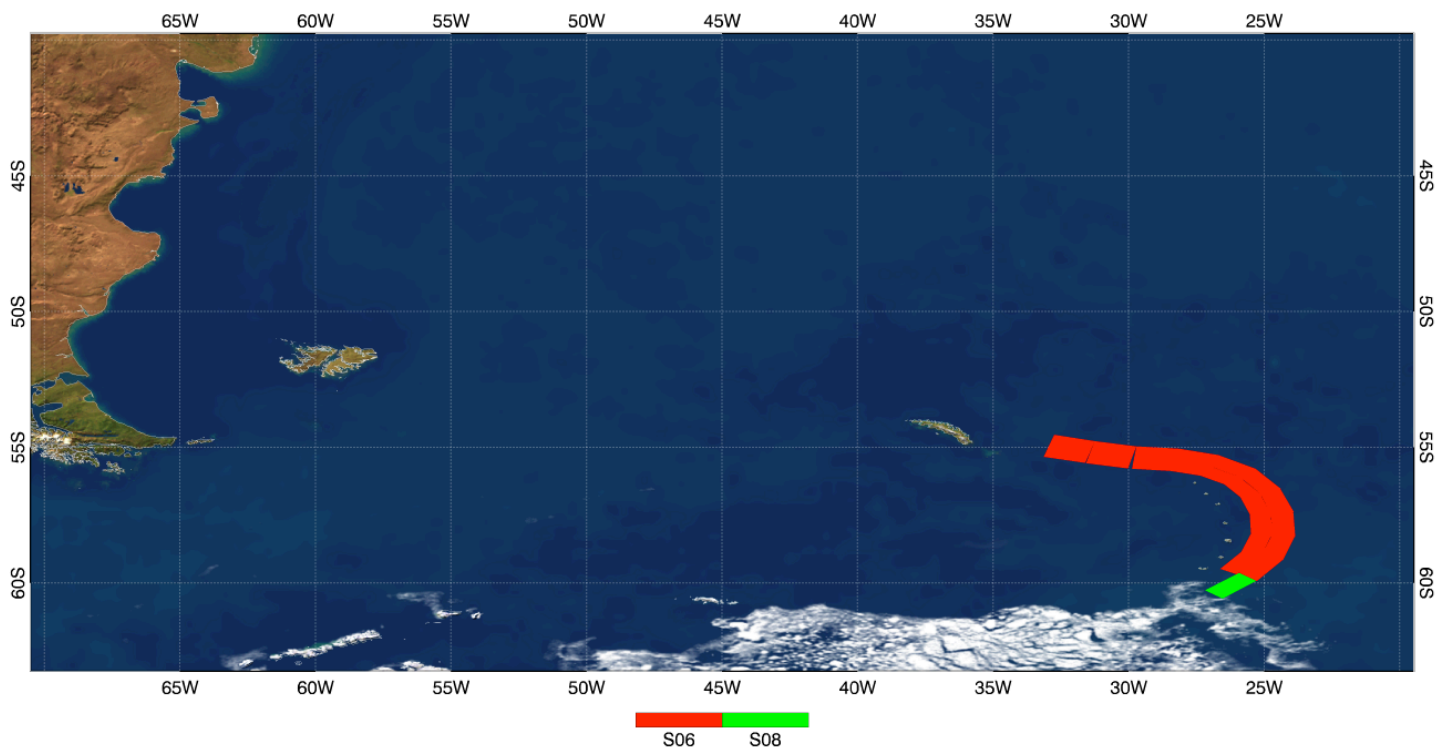




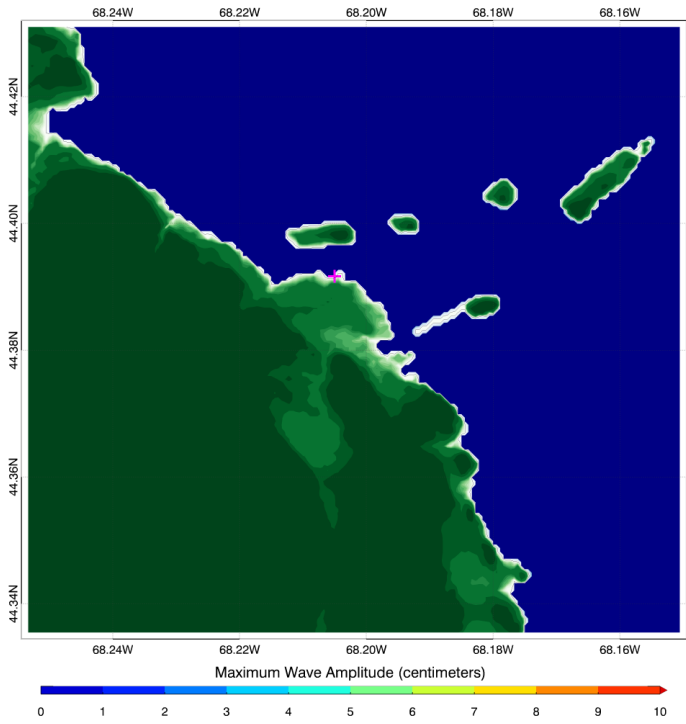




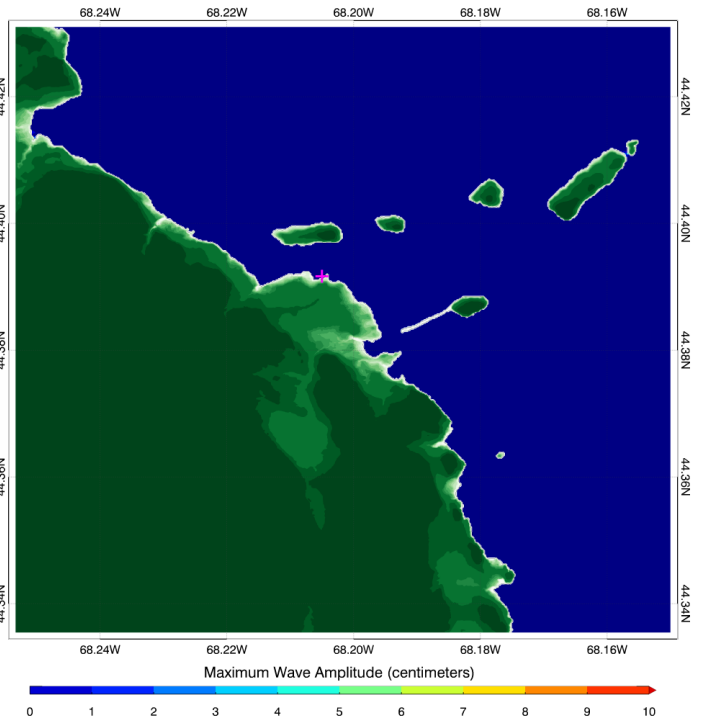


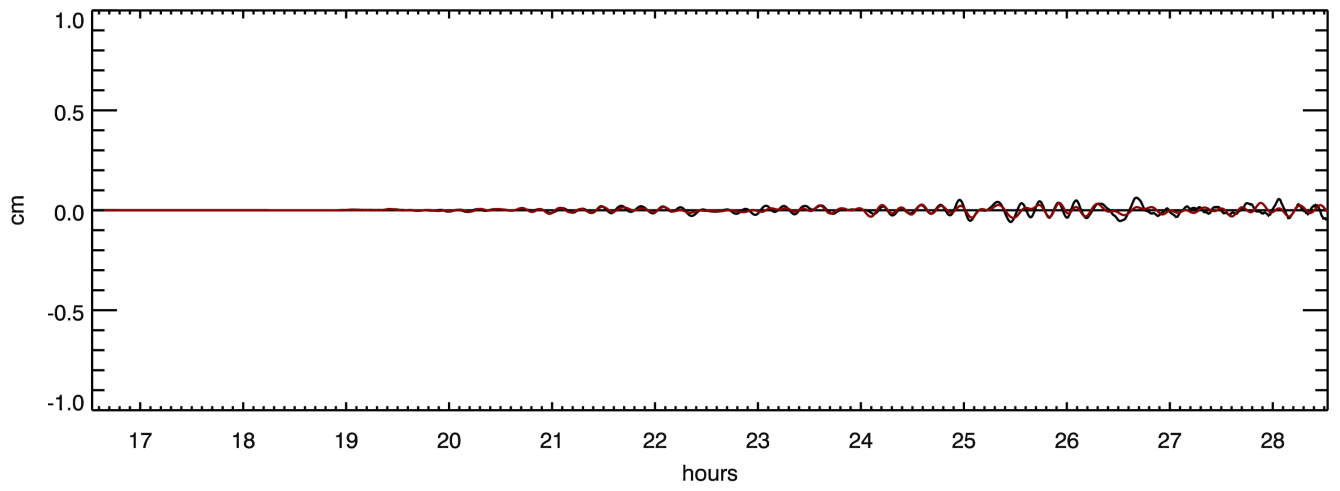


Micro scenario: C forecast grid

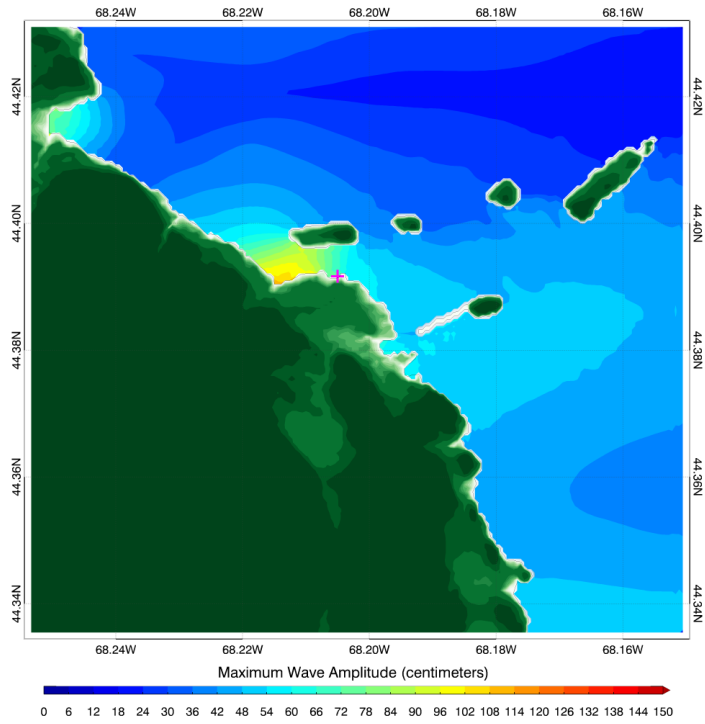


Micro scenario: C reference grid

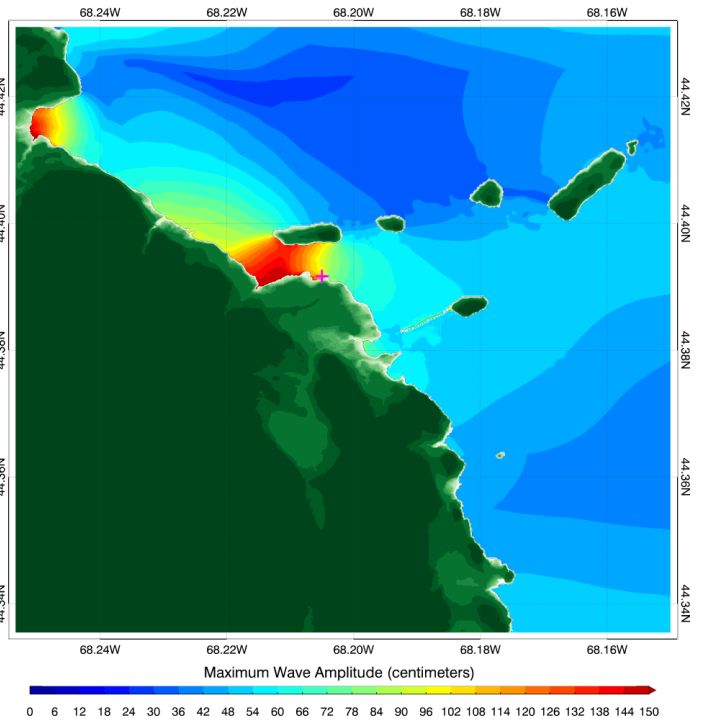


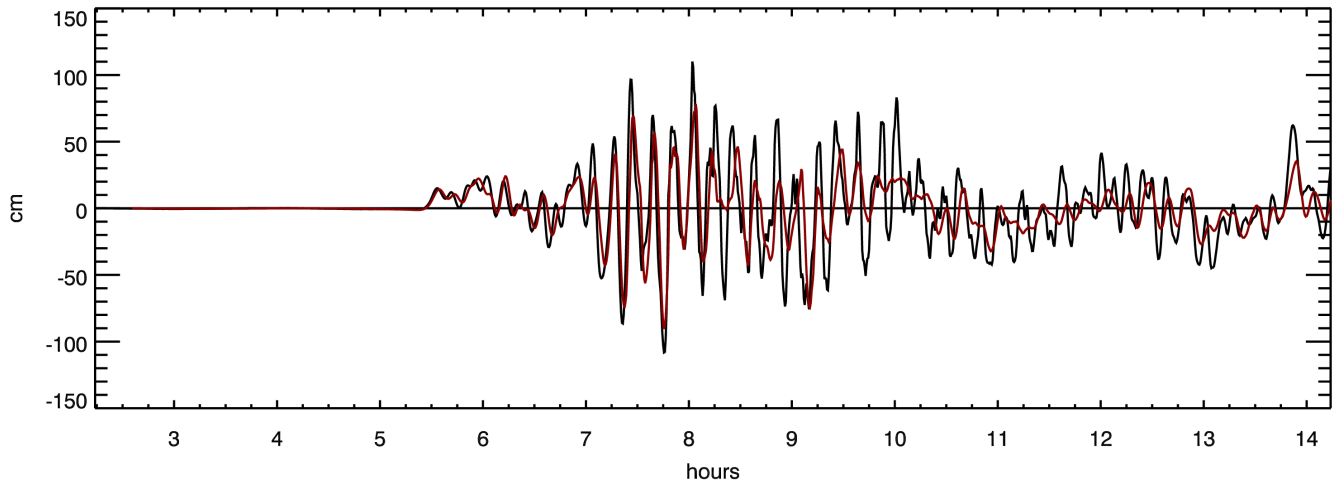


Scenario 01: C forecast grid

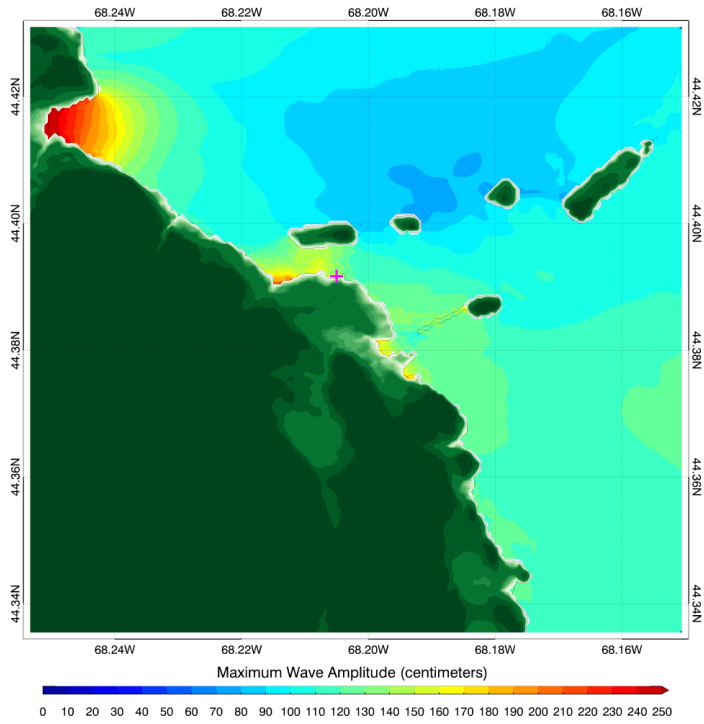


Scenario 01: C reference grid

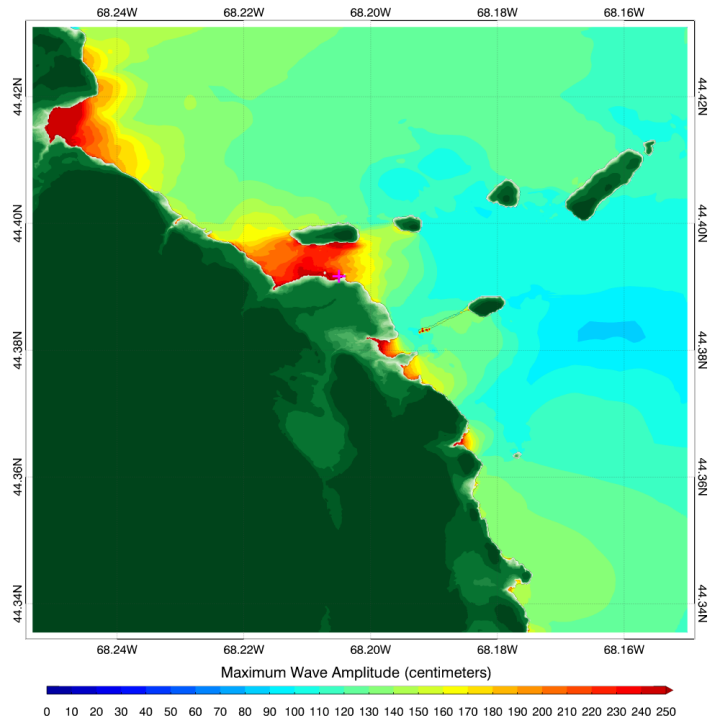


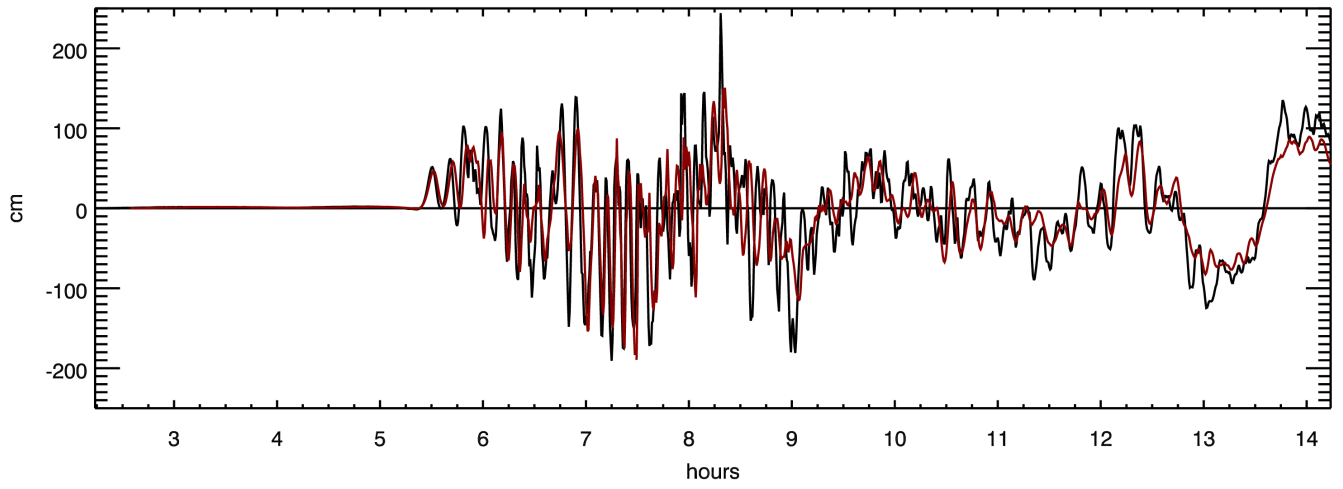


Scenario 02: C forecast grid

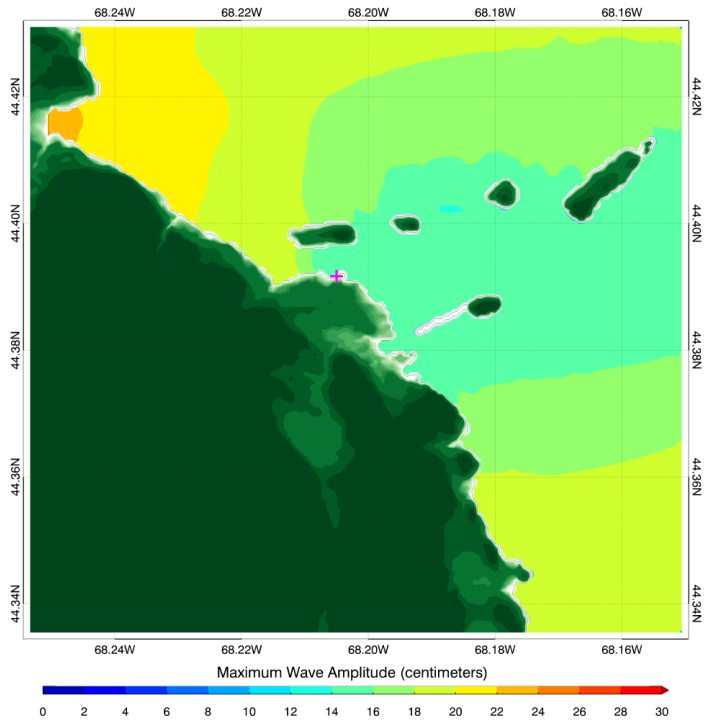


Scenario 02: C reference grid

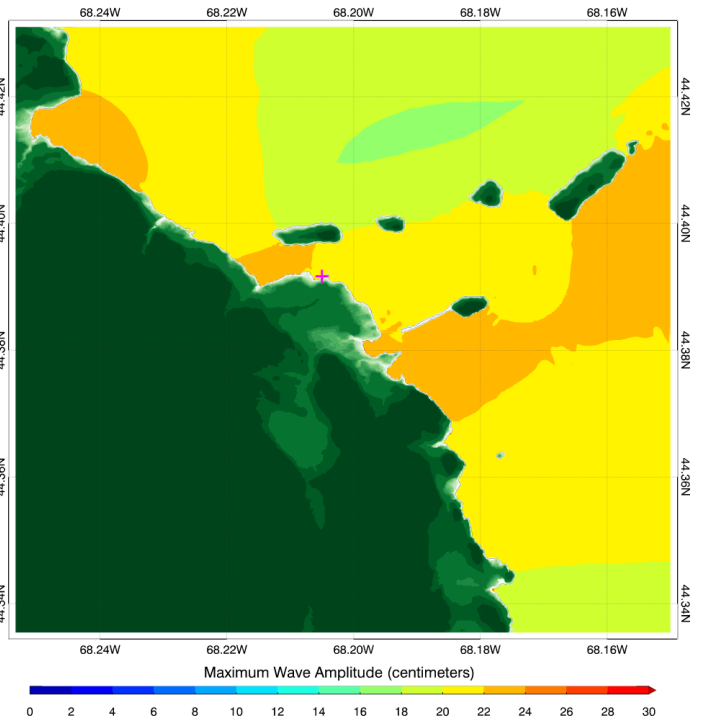


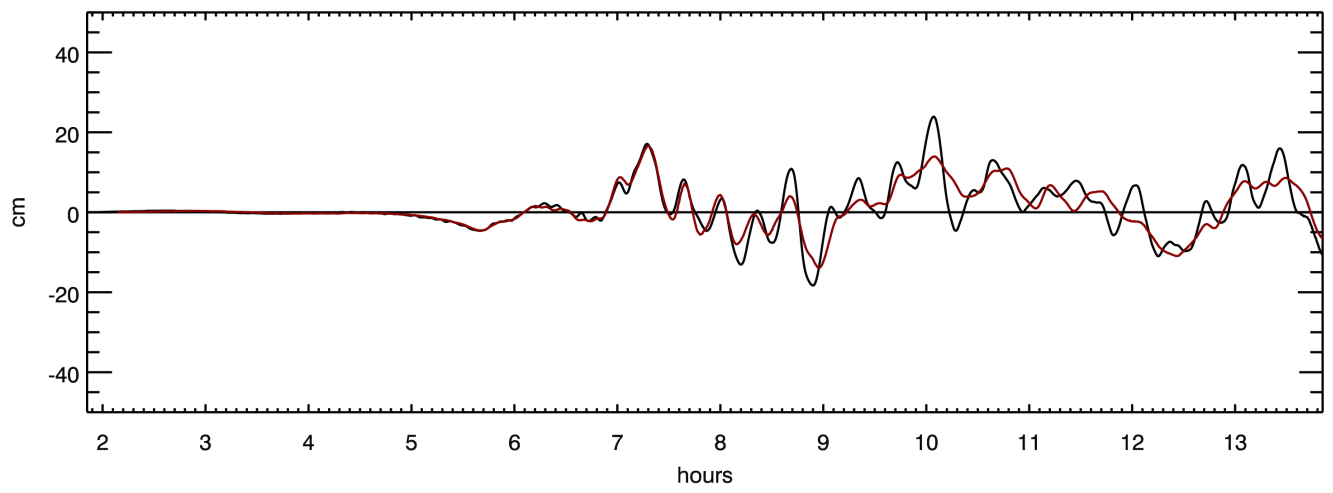


Scenario 03: C forecast grid

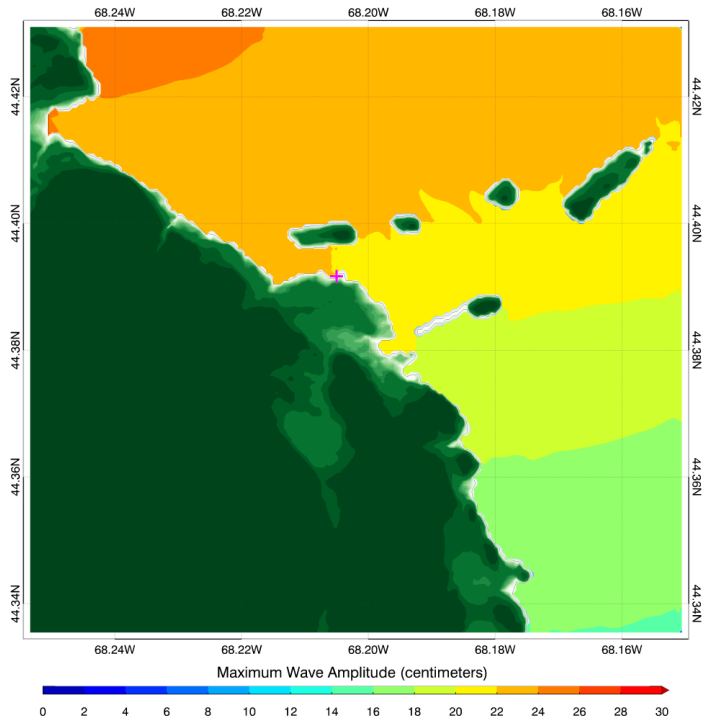


Scenario 03: C reference grid

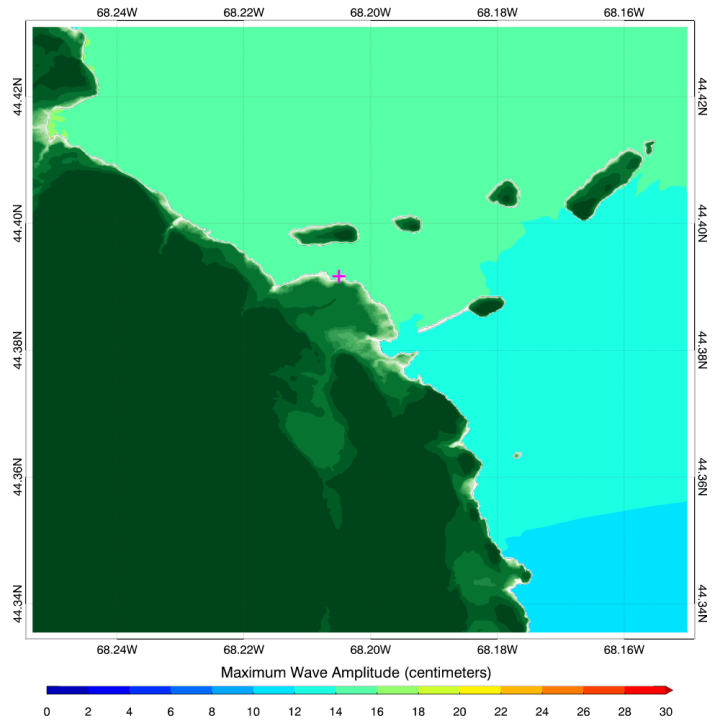


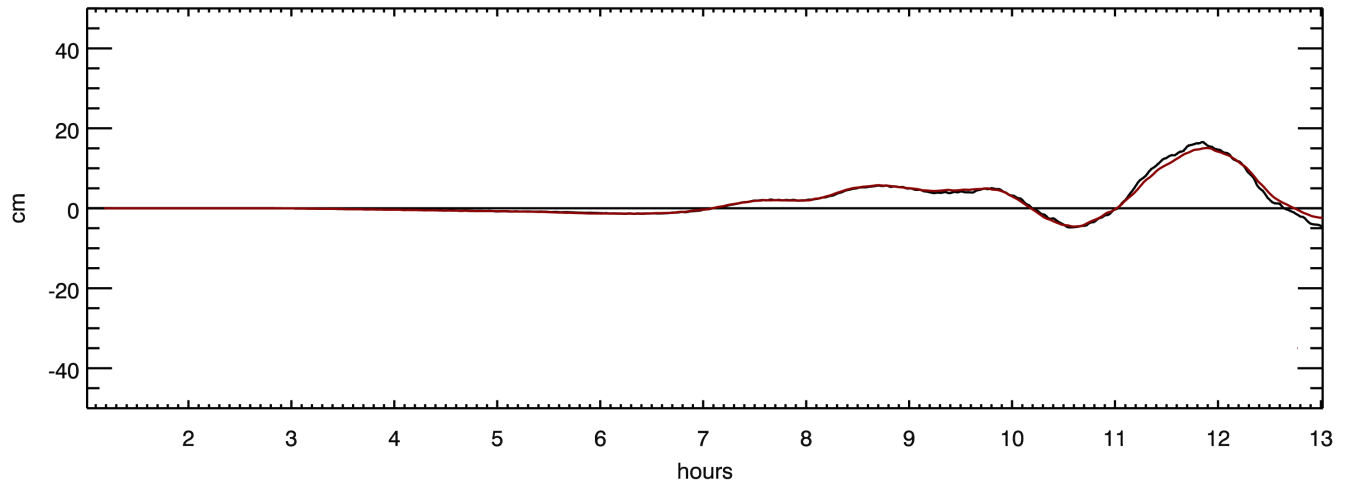


Scenario 04: C forecast grid

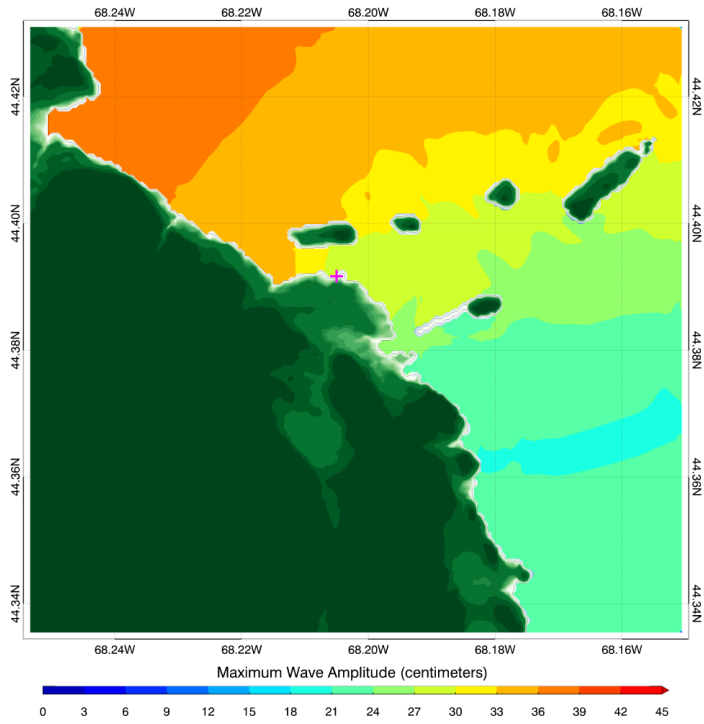


Scenario 04: C reference grid

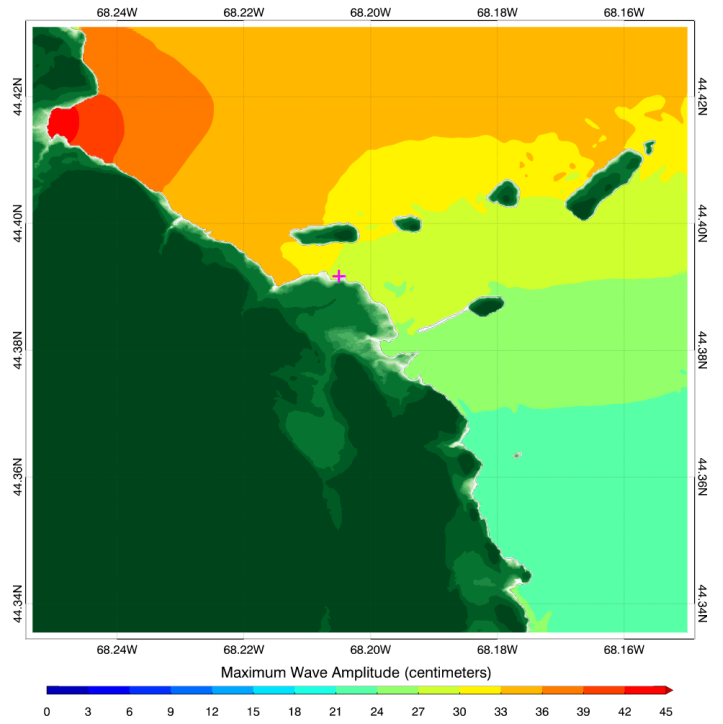


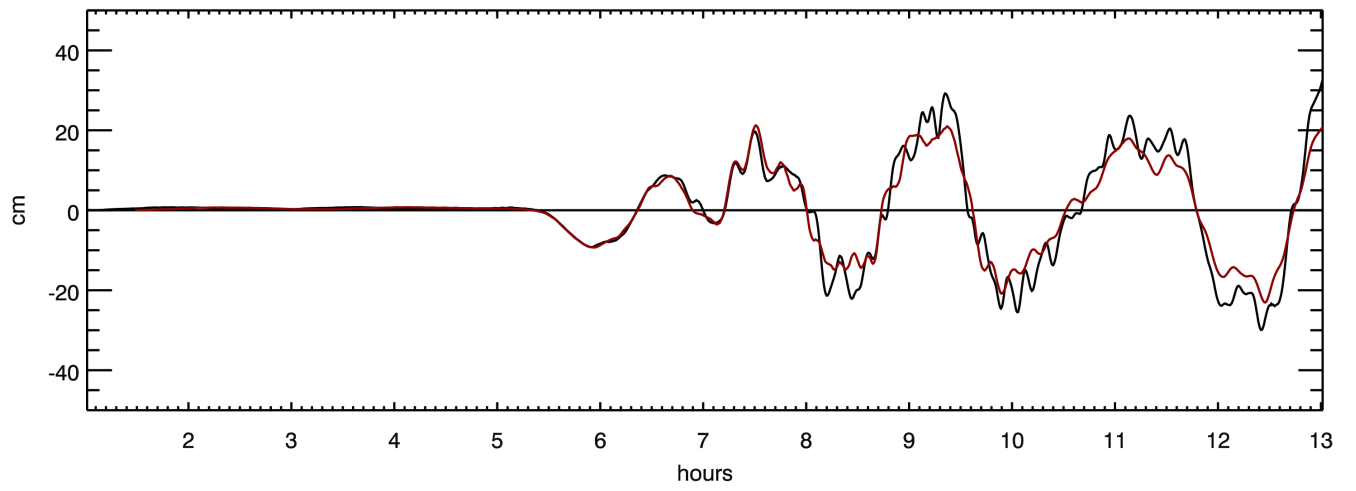


Scenario 05: C forecast grid

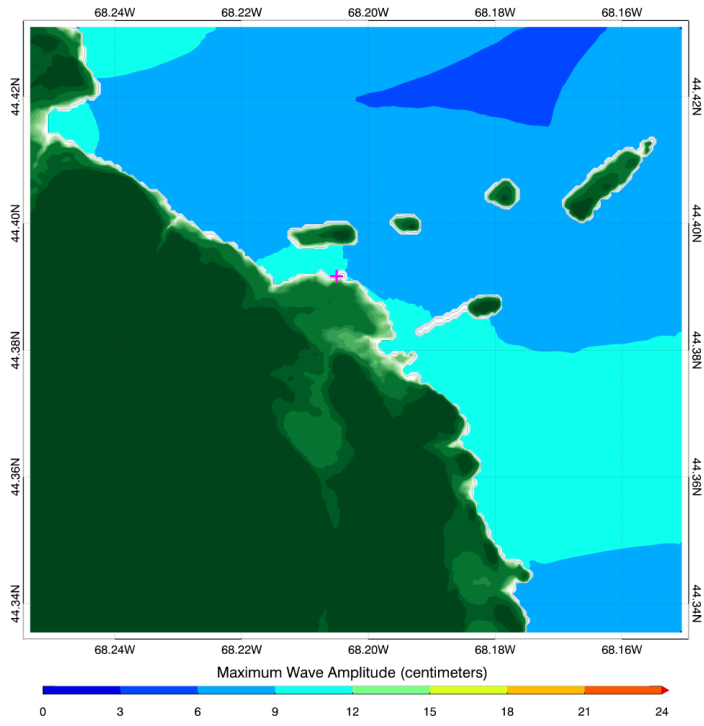


Scenario 05: C reference grid

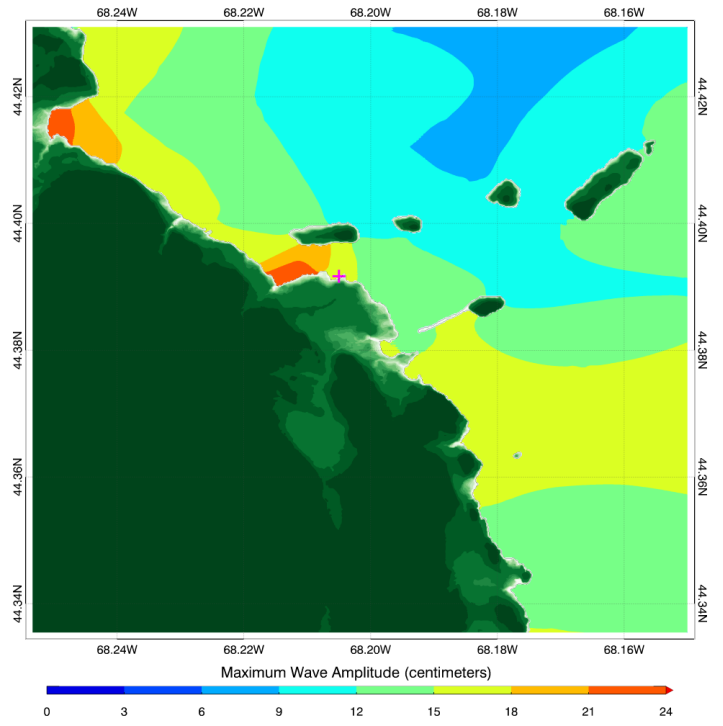


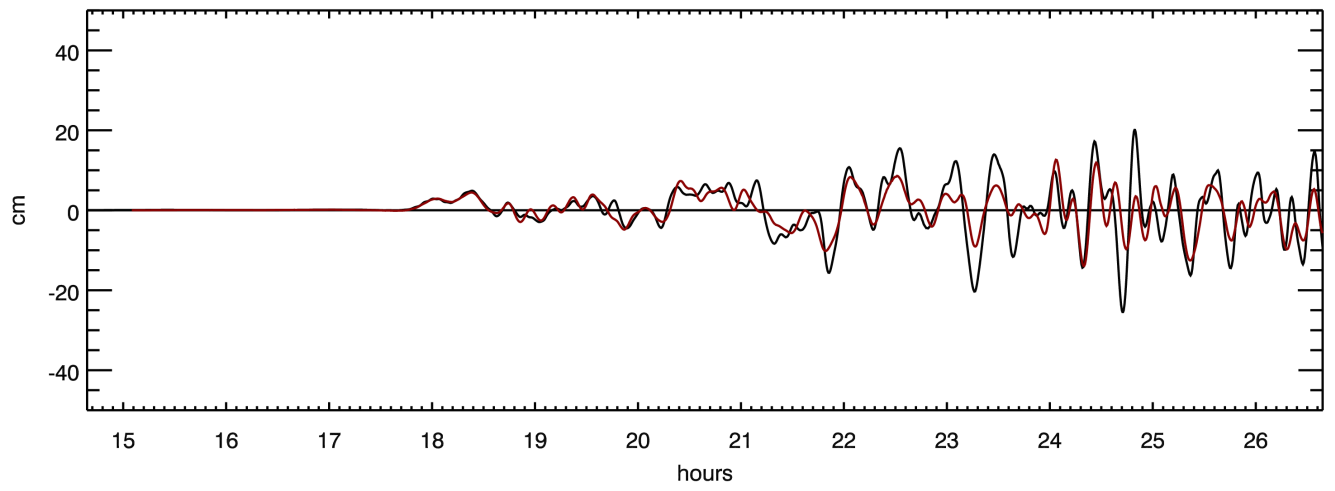


Scenario 06: C forecast grid

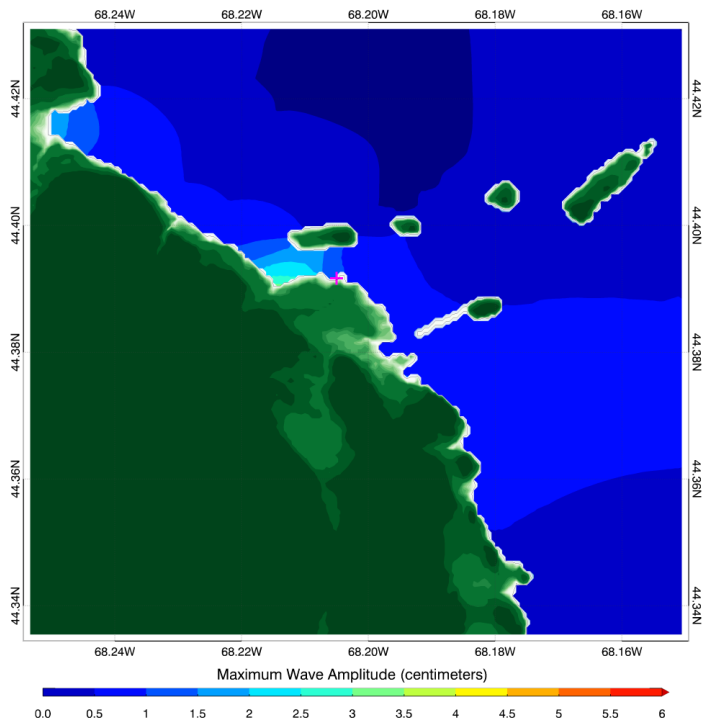


Scenario 06: C reference grid





Scenario 07: C forecast grid



Scenario 07: C reference grid

